Research Paper

GEOSPHERE

GEOSPHERE, v. 18, no. 2

https://doi.org/10.1130/GES02312.1

16 figures; 2 tables

CORRESPONDENCE:
simon.buckley@norceresearch.no

CITATION: Kurz, T.H., San Miguel, G., Dubucq, D., Kenter, J., Miegebielle, V., and Buckley, S.J., 2022, Quantitative mapping of dolomitization using close-range hyperspectral imaging: Kimmeridgian carbonate ramp, Alacón, NE Spain: Geosphere, v. 18, no. 2, p. 780–799, https://doi.org/10.1130/GES02312.1.

Science Editor: Shanaka de Silva
Associate Editor: Francesco Mazzarini

Received 7 July 2020
Revision received 12 August 2021
Accepted 10 November 2021

Published online 4 February 2022

Quantitative mapping of dolomitization using close-range hyperspectral imaging: Kimmeridgian carbonate ramp, Alacón, NE Spain

Tobias H. Kurz[1,*], Galo San Miguel[2], Dominique Dubucq[2], Jeroen Kenter[2], Veronique Miegebielle[2], and Simon J. Buckley[1]

[1]NORCE Norwegian Research Centre, P.O. Box 22 Nygårdstangen, N-5838 Bergen, Norway
[2]TotalEnergies SE, Avenue Larribau, 64000 Pau, France

ABSTRACT

Geological models from outcrop analogues are often utilized as a guide, or soft constraint, for distributing reservoir properties in subsurface models. In carbonate outcrops, combined sequence stratigraphic, sedimentological, and petrographic studies constrain the heterogeneity of geobodies and diagenetic processes, including dolomitization, at multiple scales. High-resolution digital outcrop modeling further aids geometric mapping, geobody definition, and statistical analysis, though its usefulness for detailed mineralogical and lithological mapping is limited. Hyperspectral imaging offers enhanced spectral resolution for mapping subtle mineralogical differences. In both outcrops and subsurface, differences in carbonate composition can provide key information for distributing porosity and permeability, yet this mapping is highly challenging in field studies due to access difficulties, visible material differences, and sampling resolution. Spectral analysis of limestone–dolomite ratios conducted in laboratory studies indicates theoretical measures for quantitative identification and mapping of dolomite degrees within carbonate rocks. In this study, close-range hyperspectral imaging is applied to outcrops of the Alacón Member, Barranco del Mortero, northeastern Spain, to identify exposed limestone–dolomite geobodies and to quantify the degree of dolomitization across outcrop faces. Hyperspectral imaging is supplemented with photogrammetric outcrop modeling, field spectroscopy, and laboratory sample analysis for empirical validation and uncertainty analysis. Hyperspectral mapping shows that earlier fieldwork utilizing visual inspection of difficult to access outcrop surfaces had overestimated the amount of dolomite in the outcrop. Results indicate that hyperspectral imaging identified dolomite bodies more accurately and reliably than conventional field methods and facilitates the mapping of dolomite contribution in areas modified by dedolomitization, where dolomite content changes by more than ~20%.

Simon Buckley https://orcid.org/0000-0001-8680-8286
*Present address: Geological Survey of Norway, Postboks 6315 Torgarden, N-7491 Trondheim, Norway

INTRODUCTION

Geological, depositional, and diagenetic models from outcrop analogues are crucial for the energy industry, as they provide continuous geological attributes for estimating subsurface trends in rock characteristics and quality parameters at a range of scales and thus contribute to reduced uncertainty and complexity (e.g., Kerans et al., 1994; Asprion and Aigner, 2000; Jennings, 2000; Grammer et al., 2004; Buckley et al., 2010; Kenter et al., 2010; Chesley et al., 2017). In carbonate reservoirs, high-resolution integrated analysis (sequence stratigraphic, sedimentological, and petrographic studies) and modeling are typically used to define the spatial distribution of sedimentary heterogeneities (Agar and Geiger, 2014), which in turn can constrain the distribution of porosity-enhancing diagenetic processes. Currently, numerical modeling is fundamental to carbonate outcrop characterization (Burgess, 2013; Nader et al., 2013; Hönig and John, 2015). This can be enhanced by digital outcrop modeling. Terrestrial laser scanning (lidar) and photogrammetry are frequently used to obtain highly accurate 3-D representations of outcrop surfaces, which allow geologists to map and quantify carbonate rocks (e.g., Buckley et al., 2008; Buckley et al., 2010; Hodgetts, 2013; Bemis et al., 2014).

Mapping lithology and mineralogy in outcrops is especially important when mineralogical associations are controlled by porosity-enhancing or porosity-occluding diagenetic events, such as dolomitization and dedolomitization processes (Swart et al., 2005; Lindsay et al., 2006; Al-Emadi et al., 2009; Morad et al., 2012; van Koppen et al., 2015; Schoenherr et al., 2018). In many outcrop studies, mapping and quantifying mineralogy is desirable for improved understanding of the diagenetic history and for differentiating facies that may exhibit variations in petrophysical properties, such as permeability or porosity. However, this differentiation is often limited because methods such as visible field observation, simple quantitative tests (e.g., calcimetry tests or staining methods), and costly lab analysis of samples do not allow extensive quantitative information to be retrieved. Mapping and quantifying spatial variations in rock characteristics is a common problem in outcrop studies; such efforts are hampered by accessibility issues, difficulties in achieving representative sampling, and spatial uncertainty between sampling locations. Mineral composition, and therefore facies properties, can rapidly change over short distances without showing significant color variations in the field. Conventional outcrop description often

requires sampling for mineral characterization, performed through thin section analysis, X-ray diffraction (XRD), electron microscopy, or methods such as grain density (GD) analysis or calcimetry. However, the multiscale heterogeneity of a carbonate unit is often insufficiently captured due to limited sampling coverage. While digital outcrop models allow geologists to conduct interpretation and mapping based on conventional visible red, green, blue (RGB) or lidar reflectance channels, published studies only offer empirical information for studying outcrop composition (e.g., Franceschi et al., 2009; Burton et al., 2011).

The emerging method of high-resolution, close-range hyperspectral imaging (HSI) has been shown to add value in characterizing outcrop composition to address challenges including (1) mapping and quantifying mineralogical changes consistently over an entire outcrop, (2) guiding representative sampling strategies, (3) differentiating remotely between rocks with subtle mineralogical differences that otherwise would require extensive laboratory sample analysis, and (4) gaining mineral information from inaccessible outcrop sections. Several studies have established and assessed workflows for the data collection, processing, and exploitation of close-range HSI for outcrop studies (e.g., Kurz et al., 2008, 2013; Murphy et al., 2014; Krupnik et al., 2016; Lorenz et al., 2018). Workflows often include integration with 3-D digital outcrop models to georeference and scale the hyperspectral imagery to assist quantification and validation and to utilize the geometric information as input for hyperspectral image processing (e.g., Kurz et al., 2011; Buckley et al., 2013).

The value of close-range HSI for outcrop studies has been demonstrated in a variety of geological materials and settings. Kurz et al. (2012) mapped outcrops in a carbonate quarry and differentiated limestone and several dolomite types based on varying iron and manganese content. Murphy et al. (2014) mapped clay types and distributions using spectral feature extraction. Denk et al. (2015) used close-range HSI to map minerals and elemental composition within historical iron and steelwork spoil. Krupnik et al. (2016) analyzed platform carbonates and used laboratory spectrometry of material mixtures created using mineral powders of non in situ minerals to calibrate the outcrop spectral measurements. Kurz et al. (2017) reported the application of HSI for heterogeneity characterization of the Opalinus clay in Switzerland in a tunnel-scanning setup.

Although these studies have demonstrated the potential of HSI for outcrop characterization, in particular for calcite–dolomite differentiation in carbonate rocks, very little work has been performed on quantitative mapping of dolomite, i.e., quantifying different amounts of dolomite distributed within an outcrop exposure. Minerals have distinguishing spectral signatures (e.g., Clark et al., 1990, 1993) that can be used to identify and map them. Diagnostic carbonate absorption features within the short-wave infrared (SWIR) spectral range occur as overtone and combination tones caused by fundamental vibration of the carbonate ions (CO_3^{2-}) within the crystal lattice (e.g., Hunt and Salisbury, 1971). The carbonate absorption bands within the SWIR spectral range are positioned within in the ranges of 2500–2550 nm, 2300–2350 nm, 2120–2160 nm, 1970–2000 nm, and 1850–1870 nm (Fig. 1), where the first two ranges are the strongest, and absorption intensity decreases with shorter wavelength (e.g., Hunt and Salisbury, 1971; Clark et al., 1990). Gaffey (1986) reports two additional weak absorption bands in carbonates at 2230–2270 nm and 1750–1800 nm. Due to differences in chemical composition and crystal lattice, the carbonate absorption bands are slightly shifted toward shorter wavelengths for dolomite (Fig. 1; Gaffey, 1986; Clark at al., 1990). For outcrop (outdoor) hyperspectral image analysis, atmospheric absorption makes the bands between ca. 1350–1430 nm, 1800–1950 nm, and 2480–2550 nm unusable for mineral identification, and weak carbonate bands may be difficult to observe when noise and material mixture effects are present. The latter are caused by varying material compositions within the footprint of a single pixel at the imaging distance used, which is typically several centimeters for current HSI SWIR sensors operating at ranges of <100 m.

The pronounced carbonate absorption feature found in the region of 2300–2350 nm (referred to henceforth as "2330 nm" for simplicity) remains the

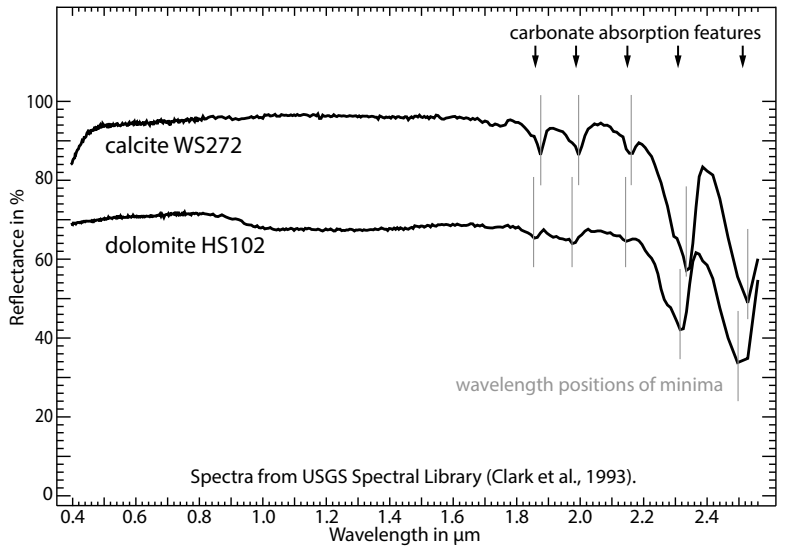

Figure 1. Example spectra for calcite and dolomite from the U.S. Geological Survey Spectral Library are shown (after Clark at el., 1993). Note the shift in the wavelength positions of the absorption minima of the calcite and dolomite spectra.

best preserved and observable "carbonate band." For this feature, Gaffey (1986) reports wavelength positions between 2333 nm and 2340 nm for calcite and 2312–2323 nm for dolomite. Carbonate absorption is also influenced by other physical and chemical parameters that include chemical composition and impurity, grain size, texture, and porosity (Crowley, 1986; Gaffey, 1985, 1986; van der Meer, 1995; Zaini et al., 2012).

Van der Meer (1995) showed that the degree of dolomitization can be determined by measuring the absolute wavelength position of the characteristic carbonate absorption features (e.g., at 2330 nm) in reflectance spectra within the SWIR spectral range. The study showed that the small shift in the wavelength position of the carbonate absorption features toward shorter wavelengths is linearly correlated with the calcite–dolomite ratio and can be used to measure dolomite abundance and thus the degree of dolomitization (van der Meer, 1995). While the dependence of the wavelength positions on the calcite–dolomite ratio was demonstrated using synthetic samples made from calcite and dolomite powders under laboratory conditions (van der Meer, 1995; Zaini et al., 2012), little work has been performed to confirm that wavelength positions of carbonate absorption bands can be applied to map dolomite abundance of carbonate rocks on outcrops.

Building on these fundamental findings, this study demonstrates the application of HSI to identify and map dolomite and limestone distribution and capture geobody shape in well-exposed but weathered outcrops of the Kimmeridgian Alacón carbonate platform of Aragón, Spain. We also quantitatively estimate the calcite–dolomite ratio of the dolomitized limestone bodies and thus map and quantify local variations in the degree of dolomitization. To achieve this aim, HSI is applied with digital outcrop modeling and supplementary control analyses (laboratory and field methods) to empirically understand the uncertainty and limitations associated with conventional field mapping and HSI approaches. Finally, the implications and new knowledge associated with the HSI results are discussed in the context of multi-scale outcrop characterization focusing on carbonate diagenetic products observable at Alacón.

CASE STUDY LOCATION AND GEOLOGICAL SETTING

The study area is located at Barranco del Mortero gully, north of Alacón village (Fig. 2), which is situated at the northeastern edge of the Iberian Range. Here, carbonate sediments were deposited within the Iberian Basin during the Kimmeridgian (Late Jurassic) and formed extensive carbonate ramps (e.g., Bádenas and Aurell, 2001). The Kimmeridgian series includes the Loriguilla and Higueruelas Formations and the intercalated Alacón Member (Aurell et al., 1994; see Fig. 2), which represents a transitional sediment succession between deeper marine sediments (Loriguilla Formation) associated with earlier rift phases and shallower (oncolite-dominated) sediments from later rift phases (Higueruelas Formation). The Alacón Member is characterized by alternating thin beds (10–40 cm) of sandstones and marls that are overlain by partially dolomitized mudstones/wackestones. One outcrop section within the Barranco del Mortero field area (Fig. 2) was selected for hyperspectral imaging. This outcrop comprised a near-vertical, well-exposed section of the Alacón Member, where dolomitization had previously been studied (Cepriá et al., 2002). These authors explain the dolomite formation with a single dolomitization event caused by reflux processes related to a stratigraphic unconformity (Cepriá et al., 2002). With reflux dolomitization models, the formation of dolomite is explained by magnesium-rich fluids formed by the evaporation of lagoon water or tidal flat water circulating through underlying carbonate sediments, which results in the transition of calcite into dolomite (Warren, 2000; Machel, 2004; Brigaud at al., 2018; Dravis and Wanless, 2018). Fluid pathways in diagenetic processes are strongly controlled by porosity and permeability, which can vary due to heterogeneous rock facies features such as bioturbation or calcretes, resulting in local alteration and dolomitization.

The distribution of limestone and dolomite in the outcrop section studied was originally mapped by the authors using conventional field methods, which resulted in the identification of four carbonate units that correspond to peloidal limestone, oncolitic limestone, limestone and marl, and dolomite (shown later in Fig. 15A). Due to the general outcrop inaccessibility, dolomite geobodies were identified based on textural observations and a distinct orange–brown color that was initially thought to reflect increased dolomite content.

DATA ACQUISITION AND METHODS

Hyperspectral Outcrop Imaging

Hyperspectral imagery was acquired during two cloud-free days in July 2017 using a HySpex SWIR-320m instrument and following the general workflow proposed by Kurz et al. (2013). The HySpex SWIR-320m instrument operates within the SWIR spectral range, between 1300 and 2500 nm, with a spectral sampling of ca. 5 nm. This acquisition configuration provides an appropriate resolution and spectral range for measuring diagnostic absorption properties of carbonates. The instrument is a pushbroom line sensor, and images are acquired by rotating the sensor around an axis parallel to the sensor line. Positioning the sensor on the valley side opposite the outcrop, at a range of around 100 m, provided a near-perpendicular viewing direction toward the outcrop surface. Due to the sensor rotation and outcrop shape, the ground sample distance (GSD) varies within a single scan image between ca. 7 cm and 10 cm depending on the imaging range. The sensor line has a field of view of 14°, which requires two scans to cover the entire height of the outcrops and a section of overlap between the images. Two spectral calibration targets (50% and 99% reflectance) were placed on the outcrops and scanned within the images for later spectral correction (Kurz et al., 2013). Validation data from ground rock sampling were acquired as described below.

3D Outcrop Model and Data Integration

Photorealistic 3-D outcrop models were used to provide a geospatial framework for all outcrop data and to georeference and integrate the HSI imagery and spectral mapping results. The outcrop models were created from handheld photography using

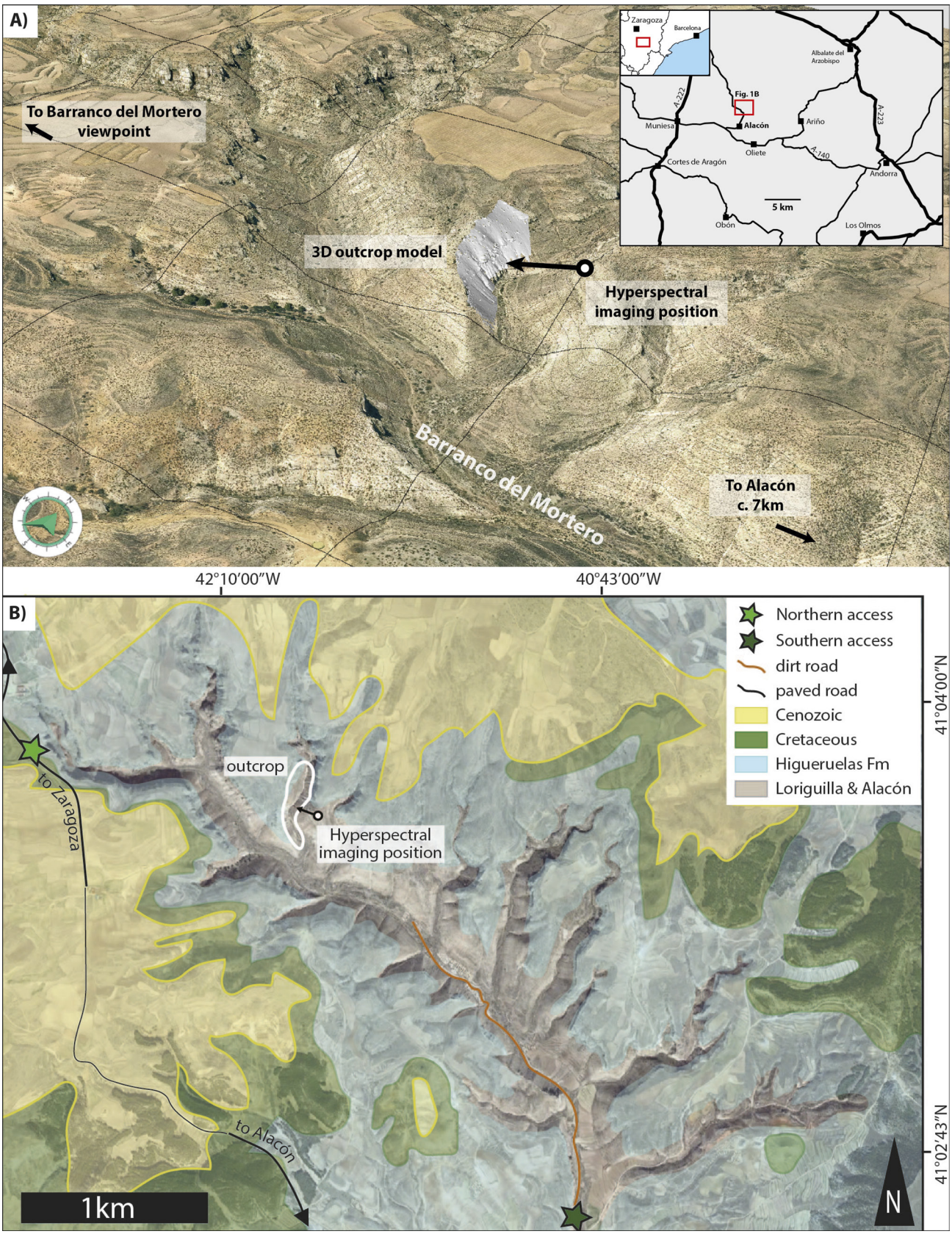

Figure 2. Map shows the outcrop location studied in the Barranco del Mortero locality, Aragón, Spain. (A) Location of field area and perspective view of field area. Contour interval is 5 m, and horizontal grid size is 500 m (inset map of Spain is courtesy of d-maps: https://d-maps.com/carte.php?num_car=2208). Red box shows the Barranco del Mortero study area. (B) Geological overview of Barranco del Mortero, which exposes continuous outcrops of the Upper Jurassic series including the Loriguilla and Higueruelas Formations and the intercalated dolomitic Alacón Member.

photogrammetry (also known as Structure from Motion [SfM]; James and Robson, 2012; Bemis et al., 2014). A Canon EOS 6D full frame digital single lens reflex (SLR) camera with an 85 mm lens was used for acquisition. Agisoft MetaShape (https://www.agisoft.com/, accessed August 2021) was used to produce a triangulated 3-D mesh textured with the high-resolution photographs, which gives a detailed and continuous representation of the outcrop exposure (e.g., Buckley et al., 2008).

The hyperspectral imagery was georeferenced by registering the spectral images within the coordinate system of the outcrop models based on a panoramic camera model as described in Kurz et al. (2011). Successful image registration is the basis for overlaying and covisualizing the digital outcrop models with hyperspectral imaging results (Buckley et al., 2013, 2019). The photogrammetric models were used to locate control points visible in the HSI imagery, which were then used to obtain the orientation and position of each HSI image at the time of observation. Buckley et al. (2013) report an accuracy of around one image pixel based on lidar data. Here, the resulting root mean square error was between 1.5 image pixels and 2.0 image pixels (ca. 7.5–15 cm in object space), which suggests that the photogrammetric mesh had a lower internal precision than "gold standard" terrestrial lidar data. Although it was out of the current study's scope to rigorously assess the accuracy of the photogrammetric 3-D outcrop model, the integration result affects the co-registration of ground truth data and therefore uncertainty as is discussed later. Registered hyperspectral images were textured as additional layers in the photogrammetric models (Fig. 3) and visualized using the LIME software (Buckley et al., 2019).

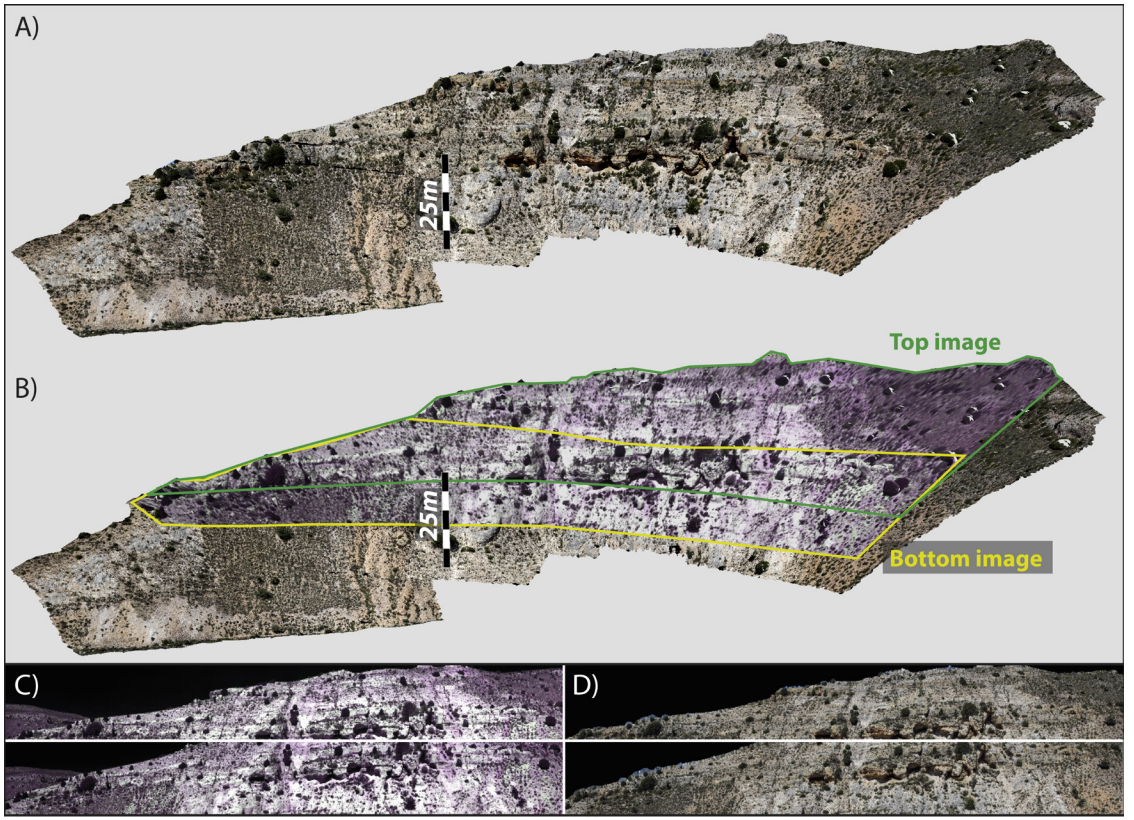

Figure 3. The outcrop studied is shown. (A) Photogrammetric 3-D model. (B) Photogrammetric 3-D model superimposed with false color hyperspectral images (bands 1734 nm, 2318 nm, and 1578 nm in red, green, blue [RGB]). Yellow/green lines delineate footprints of captured hyperspectral images (in C). (C) False color HySpex images. (D) RGB information from photogrammetric 3-D model projected into HySpex image coordinates.

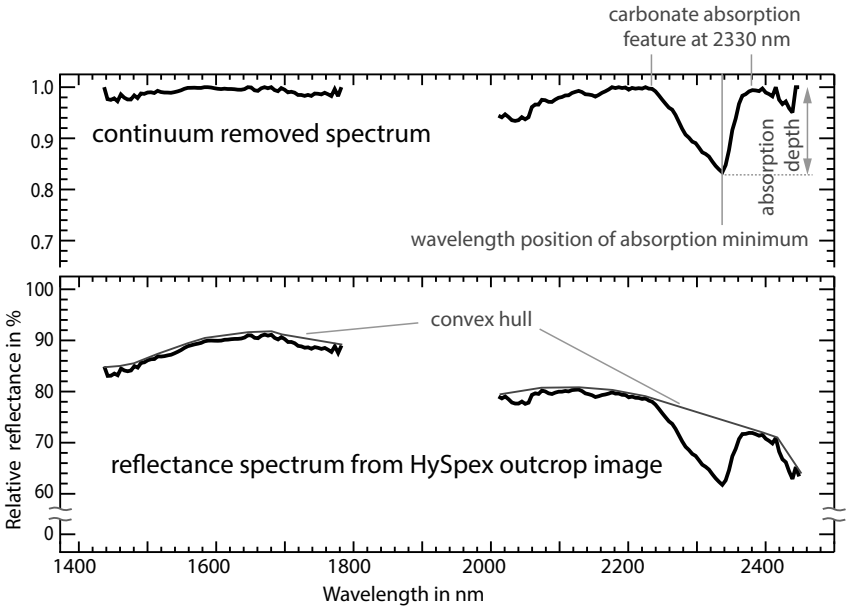

Figure 4. Normalization of spectra using continuum removal to extract absorption features allows absorption features to be compared and spectral properties, such as wavelength position and absorption depth of the absorption feature minimum, to be measured. Wavelengths of <1430 nm and 1800–1950 nm and >2480 nm are affected by atmospheric absorption and are therefore not shown.

As an additional step in the 2-D–3-D data integration, the RGB information from the digital outcrop models was back-projected into 2-D images with the same dimensions and pixel size as the hyperspectral image (Denk et al., 2015; Fig. 3D), which provided additional spectral information outside of the SWIR. The RGB bands of the Canon EOS 6D camera are centered at ca. 470 nm (blue), ca. 525 nm (green), and ca. 600 nm (red) and are much wider than the SWIR hyperspectral bands (typically >100 nm). RGB bands were combined with the SWIR data during spectral mapping, which resulted in a wider spectral range for analysis and visualization (Denk et al., 2015). Sample locations were identified within the photorealistic outcrop models. The main units identified by conventional geological field mapping were plotted on the photorealistic outcrop models, which served as the baseline interpretation for comparing hyperspectral results.

Hyperspectral Processing

Previous work has established and described in detail the processing of close-range HSI data for geological outcrop analysis (e.g., Kurz et al., 2012, 2013; Murphy et al., 2014; and Krupnik et al., 2016). Here, we describe the main steps required to obtain the hyperspectral mapping results. Spectral correction was applied using Empirical Line correction (Smith and Milton, 1999) with the 50% and 99% reflectance targets placed in the scanned areas. Areas without in situ geological information, such as scree and vegetation, were masked.

Spectral mineral mapping is based on feature extraction of diagnostic absorption properties and measures wavelength position and absorption depths as described in, for example, Murphy et al. (2014). Spectra must be normalized before absorption features can be extracted to measure these properties. Normalization was carried out using the continuum removal approach (Clark and Roush, 1984; van der Meer, 2004), which first fits a convex hull over the reflectance spectrum before dividing this convex hull by the reflectance spectrum (Fig. 4). The continuum-removed spectra are analyzed to find diagnostic absorption features that indicate the presence of specific minerals such as carbonates. The absorption features are then separated from the continuum-removed spectra to compare features from different spectra and to measure absorption parameters such as wavelength position or absorption depth at local absorption minima (Fig. 4).

Figure 5 shows five examples of spectra from the outcrop HySpex imagery for which the absorption minima of the carbonate absorption feature at 2330 nm were measured at slightly different wavelength positions. Applying the same absorption feature measurement to all pixels within the hyperspectral imagery allows for the identification and mapping of carbonate materials, as well as the linking of absorption properties to the degree of dolomitization (van der Meer, 2004; see below). The absorption depth (Fig. 4) correlates with material concentrations and therefore allows sub-pixel (relative) material abundance estimation of carbonate material for the absorption feature at 2330 nm. The wavelength position of this feature allows calcite–dolomite ratios to be estimated, though validation with ground truth data is required for absolute quantification and validation. Below, the absolute quantification of calcite–dolomite ratios is empirically established using ground truth data and linear spectral mixture modeling. Spectral angle mapper (SAM) classification (Kruse et al., 1993) was used to differentiate lithology where absorption properties, particularly wavelength position, gave unreliable results due to the absence of diagnostic absorption within the SWIR spectral range. SAM was used instead to differentiate limestone from iron-bearing limestone. The latter has a brownish weathering crust, which can result in misinterpretation as dolomite in field observation with the naked eye or using conventional visible light imagery. For efficient processing and noise suppression, maximum noise fraction (MNF) transformation (Green et al., 1988) was applied and used as input for SAM classifications.

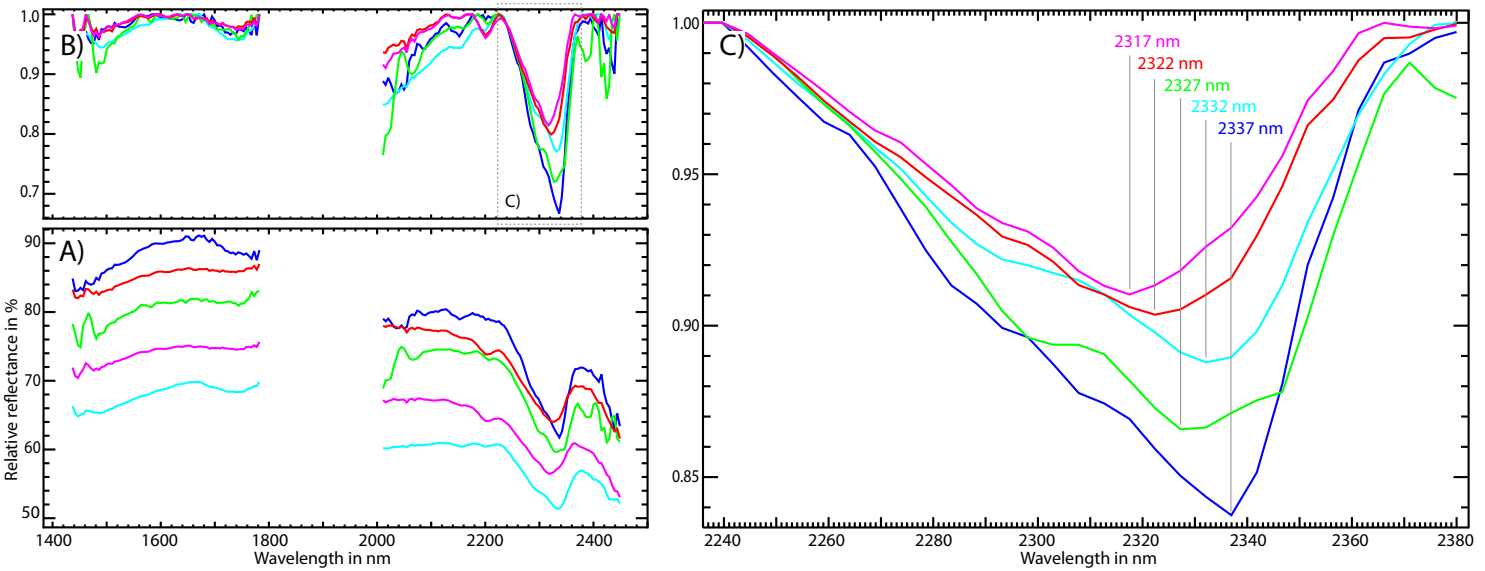

Figure 5. Wavelength positions of five HySpex spectra examples from the outcrop imagery are shown. All spectra exhibit the absorption feature at 2330 nm, which indicates the presence of carbonate. (A) Reflectance spectra. (B) Continuum-removed spectra. (C) Close-up of carbonate absorption features at 2330 nm facilitates visual comparison of wavelength position and absorption minimum of each pixel spectrum. Wavelengths of <1430 nm and 1800–1950 nm and >2480 nm are affected by atmospheric absorption and are therefore not shown.

Plug Sampling and Laboratory Sample Analysis

Rock samples (plugs) were drilled at seven accessible areas of the outcrop to provide independent mineral calibration of the HySpex imagery. Figure 6 shows the sample locations within the photogrammetric outcrop model. Note that samples were collected as part of a wider geological field campaign across the Barranco del Mortero area; original sample numbering is retained to keep the link to the acquired data set. To address the scale of the hyperspectral imagery (based on GSD) and localized geological heterogeneity, each location was sampled within a 30 × 30 cm square with four plugs in the corners and one in the center (Fig. 7) for a total of 35 plugs. Sample plugs had a diameter of 4 cm and a length between 2 cm and 7 cm. For subsequent analyses, each plug was divided into three zones, where Zone A (outcrop surface) was used for laboratory spectrometry for characterizing the weathered and fresh sample surfaces, Zone B was used for thin section preparation, and Zone C for laboratory bulk mineral analyses (grain density and XRD; Fig. 7). Of the total plugs, 32 were selected for grain density and XRD analysis (Table 1), and three thin sections (based on Zone B) were prepared.

The extracted plugs were measured under laboratory conditions using an ASD Fieldspec 4 Hi-Res spectroradiometer, a contact probe with an artificial light source covering the 350–2500 nm spectral range that provides reflectance spectra with spectral resolution of 3 nm (visible and near-infrared; VNIR, 350–1000 nm) and 8 nm (SWIR, 1000–2500 nm). Calibration was performed using a 99% Spectralon target. Reflectance measurements were performed on the weathered part of the plugs sampled as well as on the inner clean surface to assess the impact of weathering and leaching by rainwater on the reflectance spectra. In addition to the seven sampling locations, three additional samples (P1–P3) were collected for later ground truthing of the hyperspectral results; these samples were analyzed using XRD only.

RESULTS

Spectral Mineral and Lithology Mapping

Spectral mapping results are shown in Figures 8 and 9. Maps of wavelength positions of the carbonate absorption feature around 2330 nm (Fig. 8; colors represent specific wavelength positions) are diagnostic of both calcite–dolomite differentiation and calcite–dolomite ratios. The lowest wavelength positions of the absorption feature at 2330 nm, which indicate the highest dolomitization (red in Fig. 8), appear locally in relatively small areas on the photogrammetric outcrop model (shown in Fig. 10). Dolomite bodies with the highest dolomitization appear to be concentrated mainly in one horizon. It is also notable that the areas surrounding these dolomite bodies show wavelength positions that indicate intermediate dolomitization (cyan and green in Fig. 8). Geobodies exhibiting a brownish weathering surface, which are assumed to be

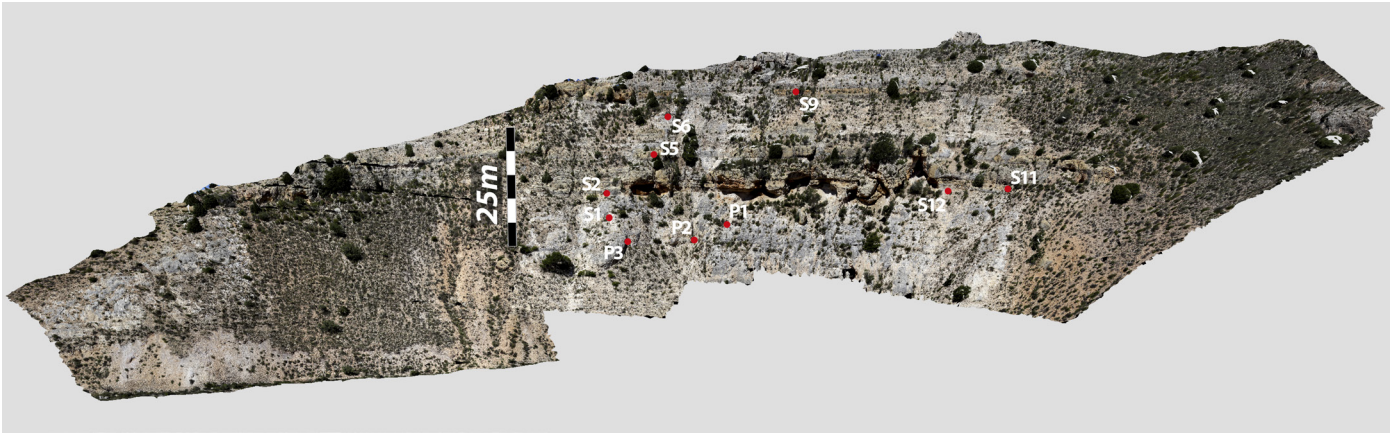

Figure 6. Red dots show the distribution of plug samples (S*n*) for laboratory analysis and additional hand specimens collected (P1–P3).

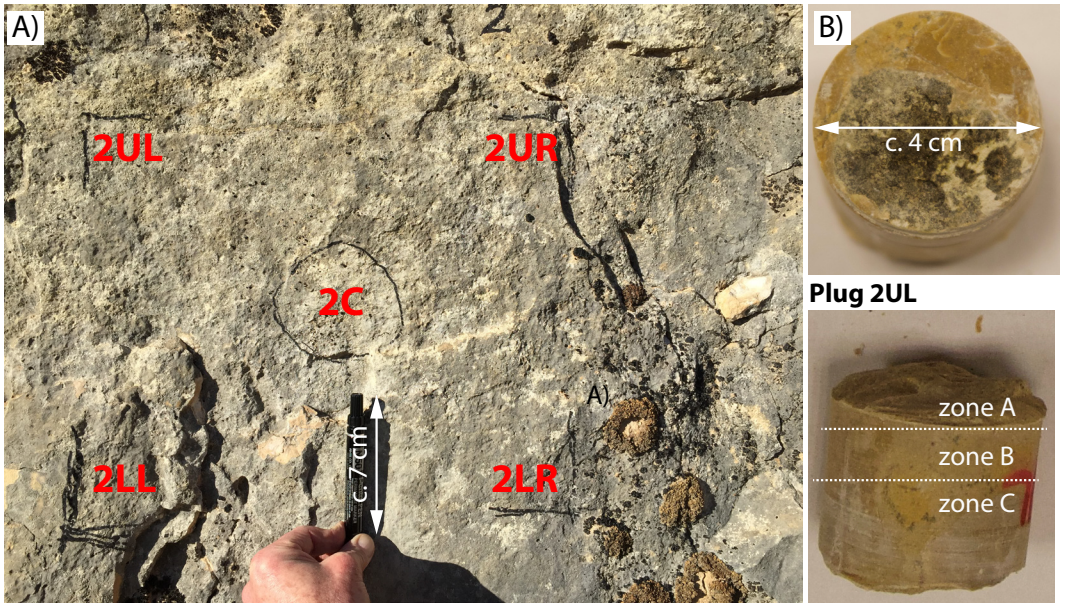

Figure 7. (A) Example of plug sampling (S2) shows the five measurement locations, which are marked upper left (UL), upper right (UR), center (C), lower left (LL), and lower right (LR). (B) The plug example is shown with the Zones A, B, and C used for different analysis.

TABLE 1. GRAIN DENSITY (GD) AND X-RAY DIFFRACTION (XRD) ANALYSIS FROM PLUG SAMPLING

Sample location	Sample ID	Grain density (GD) (g/ml)			X-ray diffraction whole-rock composition (% by weight)							
		Grain density (g/ml)	Max difference GD within sample	Ø GD in sample	Calcite	Quartz	Dolomite	Plagioclase (albite)	Total % (whole rock)	Ø calcite in sample	Ø quartz in sample	Ø dolomite in sample
1	1C	2.67	0.02	2.68	95	5	-	-	100	96	5	-
	1UL	2.68			96	4	-	-	100			
	1UR	2.67			96	4	-	-	100			
	1LL	2.69			95	5	-	-	100			
2	2C	2.60	0.15	2.65	95	5	-	-	100	94	6	-
	2UL	2.74			93	7	-	-	100			
	2UR	2.65			95	5	-	-	100			
	2LL	2.62			94	6	-	-	100			
5	5C	2.68	0.04	2.66	95	5	-	-	100	96	4	-
	5UL	2.64			96	4	-	-	100			
	5UR	2.67			96	4	-	-	100			
	5LL	2.64			96	4	-	-	100			
	5LR	2.67			95	5	-	-	100			
6	6C	2.67	0.16	2.69	100	-	-	-	100	99	3	-
	6UL	2.63			97	3	-	-	100			
	6UR	2.80			100	-	-	-	100			
	6LL	2.64			97	3	-	-	100			
9	9C	2.67	0.04	2.67	96	3	1	-	100	95	3	3
	9UL	2.67			93	4	3	-	100			
	9UR	2.65			94	3	3	-	100			
	9LL	2.69			93	3	4	-	100			
	9LR	2.66			97	3	-	-	100			
11	11C	2.78	0.03	2.76	3	1	96	-	100	3	1	96
	11UL	2.75			3	1	96	-	100			
	11UR	2.76			3	1	96	tr	100			
	11LL	2.75			3	1	96	-	100			
	11LR	2.76			2	1	97	-	100			
12	12C	2.69	0.10	2.68	94	6	-	-	100	94	6	-
	12UL	2.67			95	5	-	-	100			
	12UR	2.66			93	7	-	-	100			
	12LL	2.76			96	4	-	-	100			
	12LR	2.62			93	7	-	-	100			
P	1	-	-	-	95	5	-	-	100	95	5	-
	2	-	-	-	99	1	-	-	100	99	1	-
	3	-	-	-	98	2	-	-	100	98	2	-

Note: XRD analysis shows semi-quantitative results of the whole rock. The whole-rock composition gives the relative weight percent of each mineral in the bulk rock (tr—trace <0.5%). Dashes denote no mineral content found after analysis (for X-ray diffraction) or no measurement taken (for samples P1-3 and grain density).

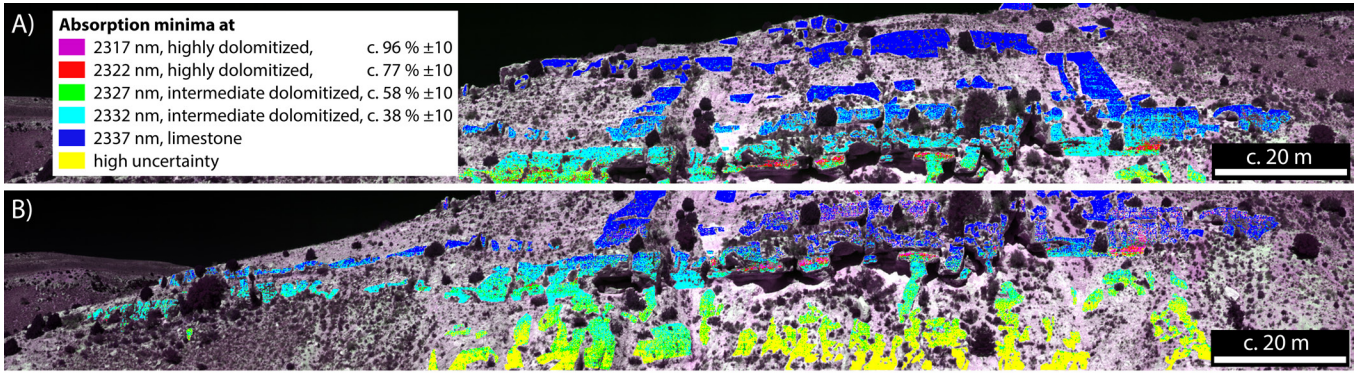

Figure 8. Spectral maps show wavelength positions of the diagnostic absorption features of carbonates around 2330 nm. (A) Top hyperspectral image; (B) bottom image. See Figure 5 for positions of the top and bottom outcrop images. Dolomite percentages are indicated based on spectral mixture modeling of XRD sample measurements.

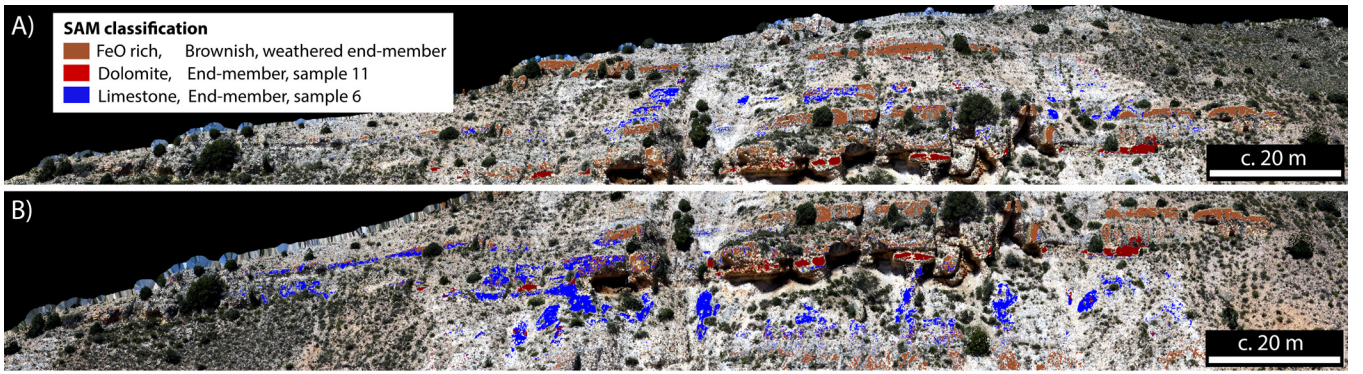

Figure 9. Spectral Angle Mapper (SAM) classification differentiates dolomite, limestone, and iron/hydroxide-rich, brownish weathering surface in the outcrop. (A) Top hyperspectral image; (B) bottom image. See Figure 5 for positions of the top and bottom outcrop images.

dolomite based on conventional field observation and color tone alone, can be easily observed, e.g., in the upper part of the outcrop. However, these areas exhibit the longest wavelength positions of the carbonate absorption feature (blue in Fig. 8), which indicates limestone composition. Based on the hyperspectral mapping, the amount of dolomite is unexpectedly low in the outcrop in comparison with the earlier observations using conventional field methods. SAM classification that included the back-projected RGB information from the digital outcrop models allowed mapping of the limestone bodies with iron oxide/hydroxide weathering (Fig. 9). Combining the carbonate absorption feature and SAM maps highlights the dolomite–limestone distribution attained by mapping diagnostic wavelength positions as well as the distribution of iron oxide/hydroxide weathering (Fig. 10). It can be also noted that the geobodies mapped with the highest dolomite abundance often occur just below the main bedding planes, and geobodies spectrally mapped as intermediate dolomite are often adjacent to the basal part of the beds. Also, geobodies exhibiting a brownish weathering surface often appear just below the bedding planes.

The low dolomite content indicated by spectral mapping is confirmed by analyses performed using the sample plugs. Table 1 shows the results from XRD, and grain density analysis performed on the seven areas sampled; of these, only sample locations 9 and 11 contain dolomite. Sample point 9 has low dolomite content (average 3% by weight) and is from the upper part of the outcrop (Fig. 6).

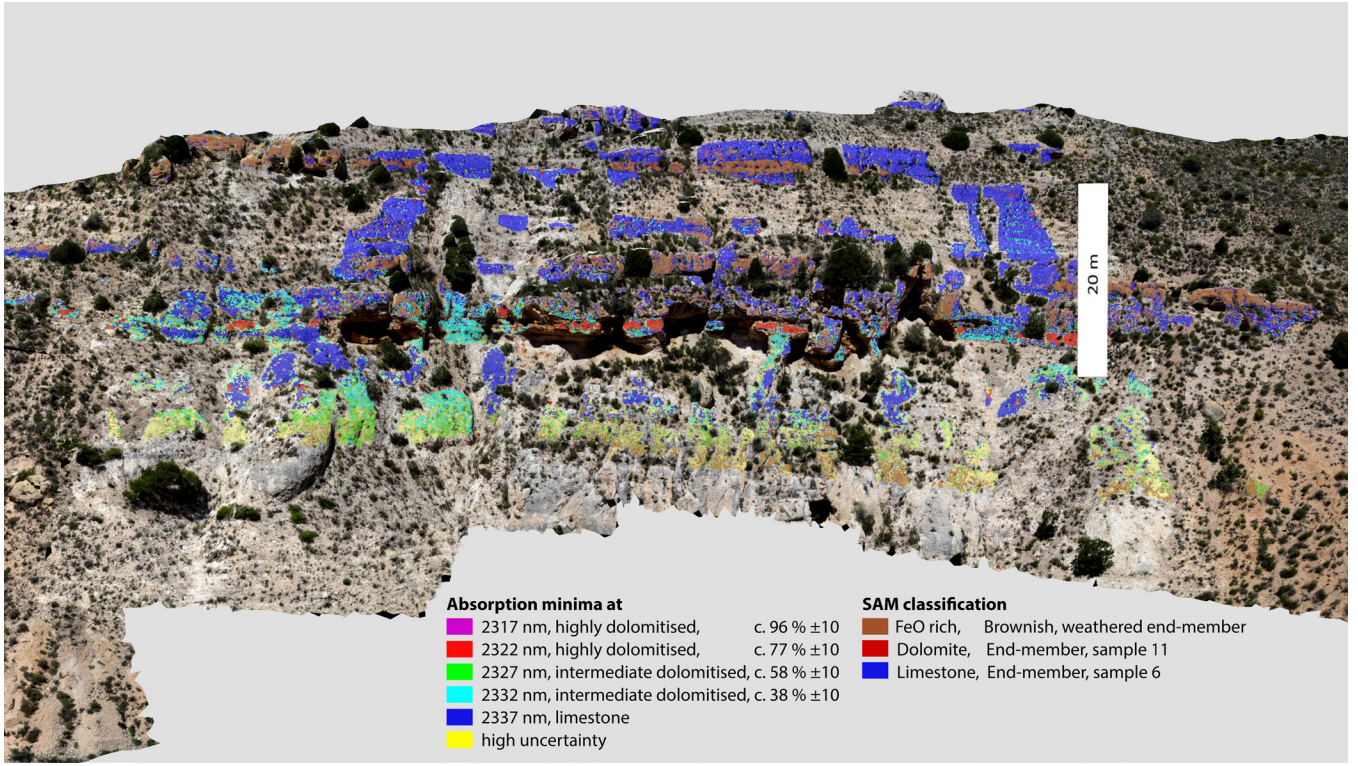

Figure 10. Photorealistic 3-D model integrates spectral map overlays of the wavelength position map (Fig. 8) and Spectral Angle Mapper (SAM) classification (Fig. 9). Dolomite percentages are indicated based on spectral mixture modeling of X-ray diffraction sample measurements.

Sample point 11 belongs to the zone with the highest dolomite content and is the only sample locality with a very high dolomite content (average 96% by weight). All other localities have calcite content of 93–100% by weight. The content of silicate minerals is low (max 7% by weight at sample points 2 and 12).

The spectra of the sample points measured from the HySpex imagery in the outcrop are shown in Figure 11. However, the exact positioning of the sample points within the HySpex imagery was hampered by the low image resolution (ca. 7 cm) and co-registration of the HSI and digital outcrop model, which may result in a slight offset between in situ and HySpex image measurements. Sample point 11 shows an offset of the carbonate absorption at 2330 nm toward shorter wavelengths, with an absorption wavelength position of 2322 nm, which is indicative of high dolomite concentration. This is confirmed by the XRD analysis of sample 11, which shows very high dolomite content (average 96% by weight) at this location.

Particularly in the lower part of the outcrop, some areas with higher uncertainty have been noted (yellow in Figs. 8 and 10). Pixels in this area do not show clear dolomite spectra; instead, the carbonate absorption at 2330 nm is modified, and double or triple absorption features appear between 2312 nm and 2332 nm though with varied wavelength positions. An example of such a spectrum with a modified carbonate absorption feature at 2330 nm and additional absorption at 2385 nm is shown in Figure 11. These spectra typically exhibit an additional absorption feature at 2385 nm, which may indicate higher uncertainties for limestone–dolomite mapping. Absorption at 2385 nm was not observed in the top image or in other areas. This modified carbonate absorption at 2330 nm could not be fully explained but causes false positives and an overestimation of dolomite. A possible explanation is that these spectra may result from material mixture, which modifies the common calcite absorption at 2337 nm. However, ground truth information (samples P1, P2, and P3 in Fig. 6) confirms limestone lithology in this area based on XRD analysis.

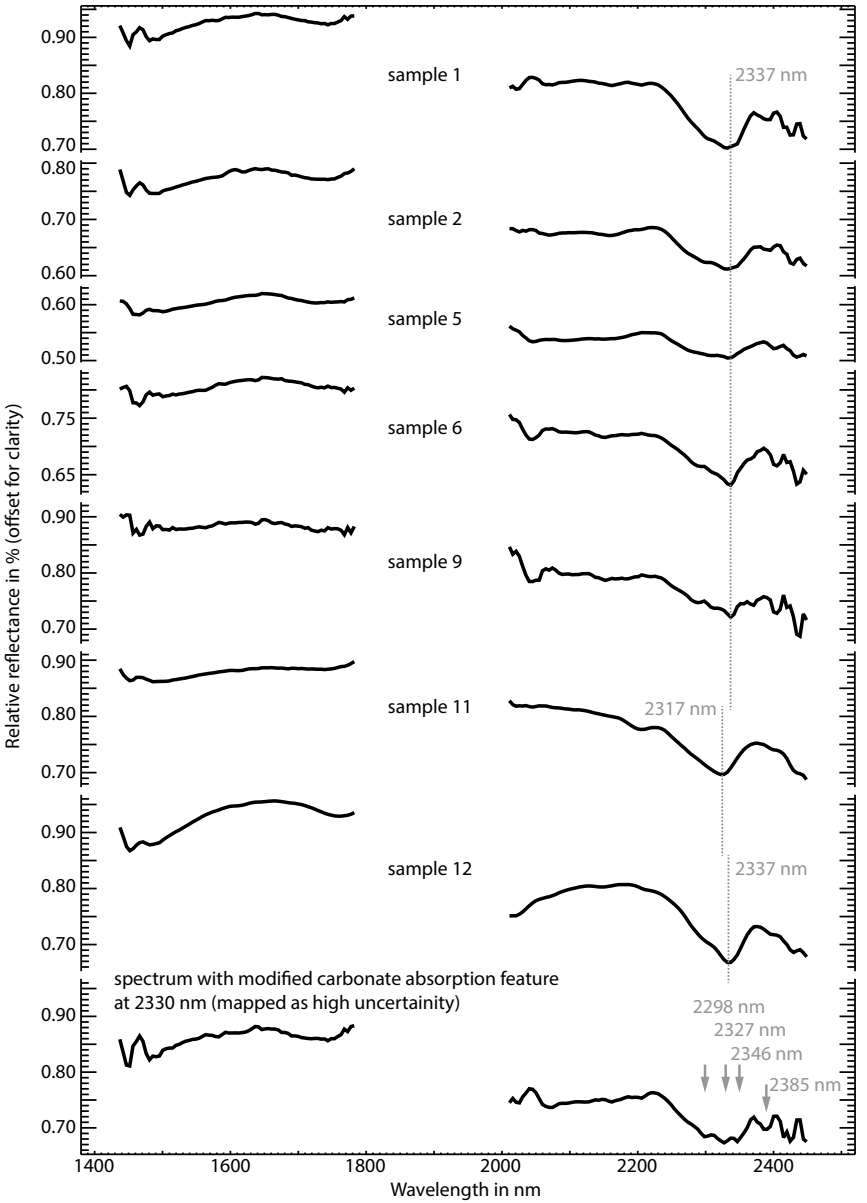

Figure 11. Spectra measured from HySpex images of sample (plug) locations show relative position and shape of the carbonate absorption features. Wavelength regions <1430 nm and 1800–1950 nm and >2480 nm are affected by atmospheric absorption and therefore are not shown. Relative reflectance in % (y-axis) is offset for clarity and to avoid the superimposition of spectra.

Sample ASD Spectroradiometer Measurement: Weathered/Non-Weathered Surface Spectra

Surface weathering can affect spectral measurements of in situ lithology. Here, the effect of weathering on the in situ rock spectra was evaluated by comparing ASD spectroradiometer measurements carried out on weathered surface and fresh cuts of collected sample plugs (Fig. 12). Spectra from weathered and fresh cut surfaces are comparable and do not show significant differences. The spectra differ mainly in the overall brightness; absorption properties such as wavelength positions are identical. The clean faces show deeper carbonate absorption features, though wavelength positions indicate no change of carbonate mineralogy from the weathered surface to the underlying clean rock. The weathered surfaces show slightly broader absorption features at 1400 nm, 1900 nm, and 2200 nm—characteristic of shale—which indicates that some shale may be partially covering the rock surface. The most striking difference between the weathered and fresh cut surfaces is a prominent iron oxide signature—similar to that of goethite or hematite—on samples 5 and 9 and to a lesser extent on sample 11 (see Fig. 13). This signature is characterized by a strong increase in reflectance at 700 nm (marked with dashed ellipse in Fig. 12) and a broad absorption feature around 900 nm. This signature is much weaker or not visible on the weathered surfaces. Most notably, samples 5, 9, and 11 were collected on geological layers interpreted (from conventional field study) to be dolomite based on their color in the field. It should be noted, however, that the iron oxide signature is within the VNIR, which is not covered by the utilized field hyperspectral imager.

CORRELATING CARBONATE WAVELENGTH POSITION WITH DOLOMITE CONCENTRATION

Van der Meer (1995) found a linear correlation between dolomite concentration and the wavelength position of the carbonate absorption features, where wavelength position shifts linearly toward

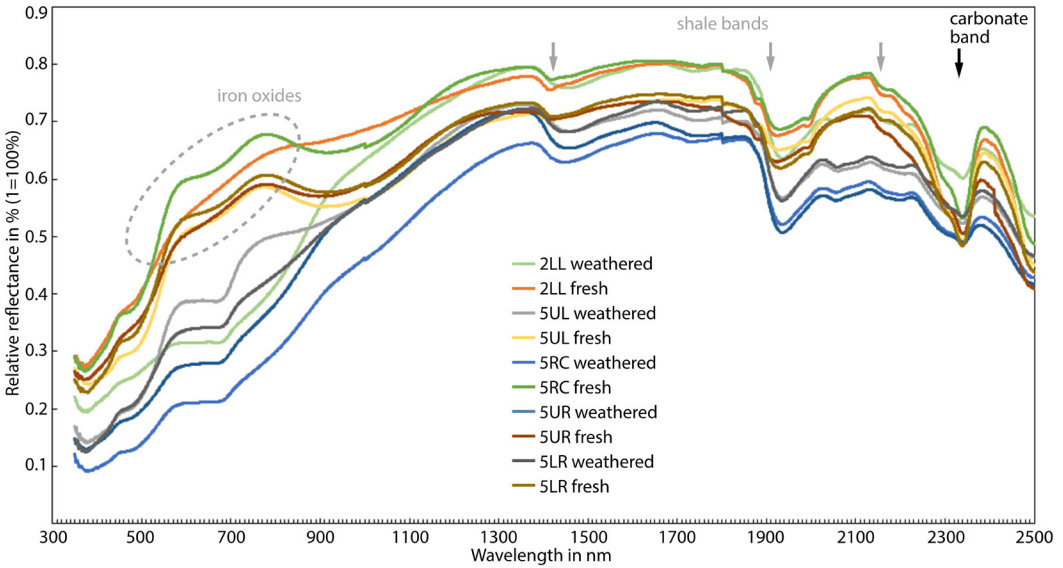

Figure 12. Plug ASD spectroradiometer measurement results from fresh and weathered surfaces are shown.

lower wavelengths with increased dolomite concentration. Therefore, correlating the wavelength position of the carbonate absorption features with empirically measured dolomite concentration permits quantification of the dolomite abundance in the outcrop and potentially provides a measure of local variation in the degree of dolomitization (calcite–dolomite ratio) that can be used in mapping from the hyperspectral imagery.

Plug samples and applied mineral analyses were assumed to be representative of the range of carbonate material present in the outcrop (based on conventional fieldwork), which was then expected to allow an empirical correlation of the spectral measurements for dolomite quantification. However, as the samples did not exhibit a wide range of dolomite concentrations, this hindered the correlation between dolomite concentration and wavelength position for the carbonate absorption feature at 2330 nm. The widest range of calcite–dolomite content is seen in sample 6 (highest calcite content with an average of 99% by weight) and sample 11 (highest dolomite content with an average of 96% by weight). The spectra of these two samples are used as spectral end-members. The wavelength positions of the carbonate feature at 2330 nm can be directly correlated with the dolomite concentration (Table 2), which corresponds to 2337 nm for sample 6 (calcite) and 2317 nm for sample 11 (dolomite).

Because dolomite is largely absent in the other plug samples, spectra for intermediate dolomite concentrations cannot be measured from the plugs themselves, so an alternative approach was applied. The spectra for intermediate dolomite concentrations were modeled by calculating linear spectral mixtures with 20% mixture steps between the spectra of sample 6 (highest calcite content) and sample 11 (highest dolomite content). Figure 14 shows the linear spectral mixture model using these samples as end-members with known calcite and dolomite concentrations. Wavelength positions of the carbonate absorption feature at 2330 nm were then extracted and measured from the mixed spectra (Fig. 14, Table 2) and used to estimate dolomite concentrations (dolomite–calcite ratios) as indicated in Figures 8 and 10. Table 2 shows the calcite–dolomite concentrations represented by the mixed spectra.

DISCUSSION

The results are discussed below with respect to the hyperspectral method and geological implications.

Scale, Spatial Resolution, and Localization

HSI offers a potential solution for mineral mapping of outcrop sections, especially for similar mineralogy, such as dolomite and calcite, which can be difficult to differentiate using the naked eye. Although conventional field and laboratory methods, such as hydrochloric acid testing (HCl) or calcimetry, are invaluable for determining mineralogical composition, sampling strategies are problematic and cannot currently address the heterogeneity and

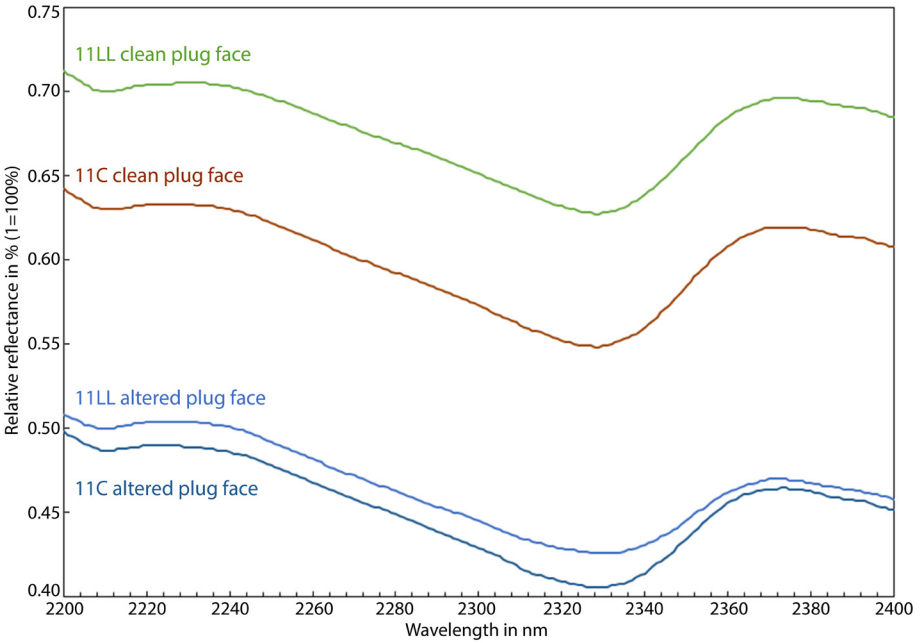

Figure 13. ASD spectroradiometer measurement results from S11 plugs (weathered and fresh surfaces) are shown. This is the only sample with a carbonate absorption feature at a lower wavelength, 2330 nm vs. 2340 nm.

distribution within an exposed and inaccessible cliff section. This study demonstrates that dolomite–calcite carbonate can be reliably differentiated using HSI. Calibrating spectral properties, such as wavelength positions with dolomite concentrations, for more quantitative mapping of calcite–dolomite ratios, remains a challenge for several reasons. It is difficult to locate centimeter-scale sample spots precisely in low-resolution hyperspectral images (ca. 7–10 cm GSD used in this study) when mineralogy may vary over short distances. Using geological samples for empirical correlation was not definitive because the samples obtained did not provide wide variability in dolomite concentration despite our best efforts to sample accessible horizons. Instead, the spectral linear mixing model with limestone and dolomite end-member spectra was required to calibrate wavelength position for different dolomite concentrations (Fig. 14; Table 2). The absorption in the mixed spectrum 80% sample 6 / 20% sample 11 appeared flatter at shorter wavelengths (Fig. 14), though wavelength position was not shifted in comparison to sample 6 (limestone) spectra. This indicates that differences in dolomite concentration of less than around 20% may not be reliably mapped from the HySpex SWIR-320m imagery. This would most likely be due to the spectral resolution of this instrument, which is at the limit of current sensor technology for field-based SWIR imaging. It also should be noted that rock spectra used in this linear model may be affected by a compositional complexity due to the presence of additional minerals (e.g., quartz, as indicated by XRD analysis), which may result in more complex mixture effects. This means that differences in dolomite concentration must be larger than ca. 20% to reliably differentiate within the HySpex SWIR-320m imagery.

Wavelength Position for Calcite–Dolomite Mixtures

The hyperspectral imagery shows, for the carbonate absorption at 2330 nm, a wavelength position of 2337 nm for carbonate rocks with 99% calcite content and 2322 nm for rocks with 96% dolomite content measured on outcrop. This results in a wavelength window of ca. 15 nm for the absorption position of limestone–dolomite mixture. The observed wavelength positions for the

TABLE 2. RELATIONSHIP BETWEEN DOLOMITE CONCENTRATIONS AND WAVELENGTH POSITIONS BASED ON LINEAR SPECTRAL MIXING BETWEEN HYSPEX SPECTRUM OF SAMPLES 6 AND 11

Sample	Mineralogy from XRD	Linear spectral mixture model	Calcite represented by spectrum (%)	Dolomite represented by spectrum (%)	Wavelength position at 2330 nm absorption	Source
Sample 6	99% calcite	100% sample 6	99		2337 nm	Measured
		80% sample 6 / 20% sample 11	79	19	2337 nm	Modelled
		60% sample 6 / 40% sample 11	59	38	2332 nm	Modelled
		40% sample 6 / 60% sample 11	40	58	2327 nm	Modelled
		20% sample 6 / 80% sample 11	20	77	2322 nm	Modelled
Sample 11	96% dolomite	100% sample 11		96	2317 nm	Measured

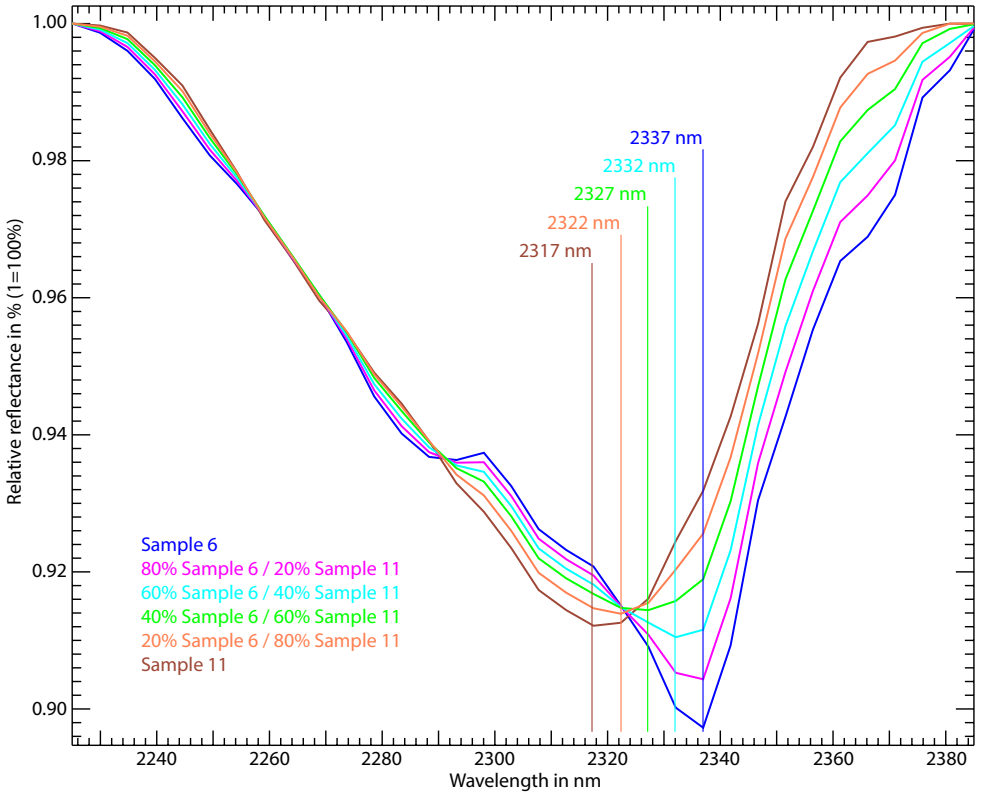

Figure 14. Wavelength positions were modeled from linear spectral mixture between HySpex spectra of Sample 6 (representing 99% calcite) and Sample 11 (representing 96% dolomite). Spectra are normalized using continuum removal.

carbonate absorption at 2330 nm agree with the observations of Gaffey (1986), who reports positions between 2333 nm and 2340 nm for calcite and 2312 nm and 2323 nm for dolomite. In contrast, the laboratory study of van der Meer (1995) observed a linear relationship between dolomite and calcite mixtures for which the absorption wavelength position for 100% calcite is at 2332 nm and the absorption wavelength position for 100% dolomite is at 2304 nm. This results in a wavelength range of over 28 nm for the absorption wavelength position of calcite–dolomite mixtures.

The offset of absolute wavelength positions can be explained by the different spectral calibrations of various sensors, observations made in laboratory versus real-world outdoor settings, and by differences in chemical composition and impurity (e.g., Gaffey, 1985, 1986; van der Meer, 1995; Zaini et al., 2012).

Spectral mapping was hindered by some unidentified absorption properties (see bottom spectrum as an example in Fig. 11) that were mapped as high uncertainty in Figures 8 and 10, which modified the carbonate absorption at 2330 nm and resulted in the overestimation of dolomite in the lower part of the outcrop. XRD analyses of samples P1–P3 confirmed limestone lithology in this part of the outcrop (Fig. 6, Table 1). Although the exact source of these spectra remains unclear, the hyperspectral mapping allows these areas to be assigned higher uncertainty, which prevents overestimation of dolomite content.

Figure 15 shows a comparison of the geological outcrop interpretation based on conventional field methods (Fig. 15A) and modified interpretation following the incorporation of the hyperspectral imaging results (Fig. 15B). Spectral mapping indicates significantly less dolomite in the studied outcrop of the Barranco del Mortero valley than was mapped by conventional field methods based on remote observations of color variation during fieldwork and from digital outcrop models. The dolomite bodies with the highest degree of dolomitization (>80% dolomite) mainly appear locally within one horizon in the outcrops (Fig. 15). Geobodies with brownish weathering colors were previously assumed to be dolomite. However, in this study, spectral mapping clearly identified some of the brownish rock bodies as limestone. The low dolomite content and limestone lithology of brownish weathered rock bodies were confirmed by laboratory analysis of ground samples and represent a significant result. The spectral mineral maps that were developed provide input for more representative sampling strategies, though sampling is still limited by access to steep outcrop sections. It can be concluded that spectral mineral mapping improved the accuracy of outcrop mapping and prevented the incorrect mapping of dolomite bodies. Furthermore, sampling was guided by hyperspectral information for verification of the highly dolomitized carbonate bodies and the iron-rich limestone bodies.

Petrographic and Diagenetic Context

The limestones of the Alacón Member were interpreted to have been affected by a single event of dolomitization at an early diagenetic stage (Cepriá et al., 2002) that affected mostly the finer sedimentary facies and resulted in micron-scale sucrosic (full process) and sparse (partial) fabrics of dolomite. This hypothesis does not explain the occurrence of multiple and vertically disconnected highly dolomitized geobodies in the

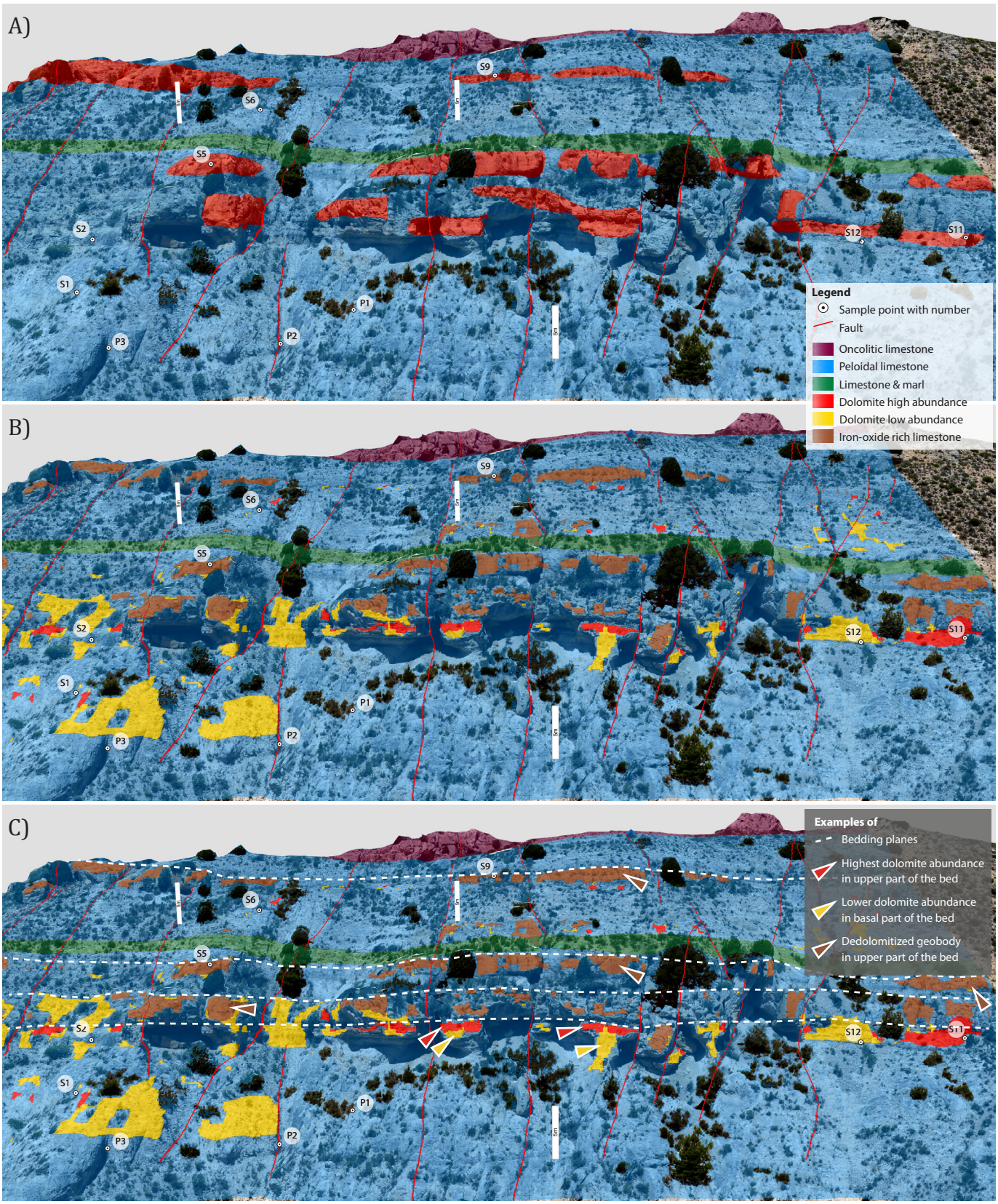

Figure 15. Original fieldwork-based mapping of dolomite geobodies in the outcrop is compared with modified distribution following hyperspectral analysis. (A) Virtual outcrop model was interpreted based on conventional geological fieldwork. (B) Interpretation modified by hyperspectral classification results shows finer differentiation of main lithologies. (C) Distribution of the altered geobodies shows the strata-bound nature of the original dolomite geobodies. Scale bars are 5 m high.

outcrop identified by the hyperspectral mapping (Fig. 15). Moreover, because the sample plugs contained less dolomite than originally assumed from the field mapping, three samples were studied in greater detail with additional methods that included thin section analysis to improve the understanding of these lithologic units and their spectral response. These samples were plug S9LL (3% dolomite by weight), which was collected from one of the brownish weathered geobodies spectrally mapped as limestone, plug S11UR (96% dolomite by weight), which exhibits the highest dolomite content through its spectral response, and plug 5C, which contains no dolomite (Fig. 16; Table 1).

From petrographic images (Fig. 16E), partial to fully replacive dolomitization processes can be observed that result in a homogeneous sucrosic micro-fabric of euhedral dolomite crystals. However, petrographic pictures of samples 9 and 11 in Figure 16 (B, C, E, and F) show similar petrographic fabric even though the dolomite contents established using XRD and grain density vary greatly. Thin sections indicate that the dolomitization exhibits a ferroan composition. In petrographic images (Fig. 16), euhedral dolomite crystals within a micritic matrix (posteriorly partially recrystallized by calcite cements) can be observed, which are linked to opaque minerals within the crystal structure (Fe-oxides), where inter-dolomite crystal porosity is fully plugged. Sample S9LL indicates 3% dolomite content, which confirms most of the petrographic rhombs visible today that transformed into calcite, while intracrystalline porosity was filled by ferric oxides. Sucrosic textures were preserved while dolomite was transformed into calcite (Figs. 16F–16I). Ferric oxides and other opaque

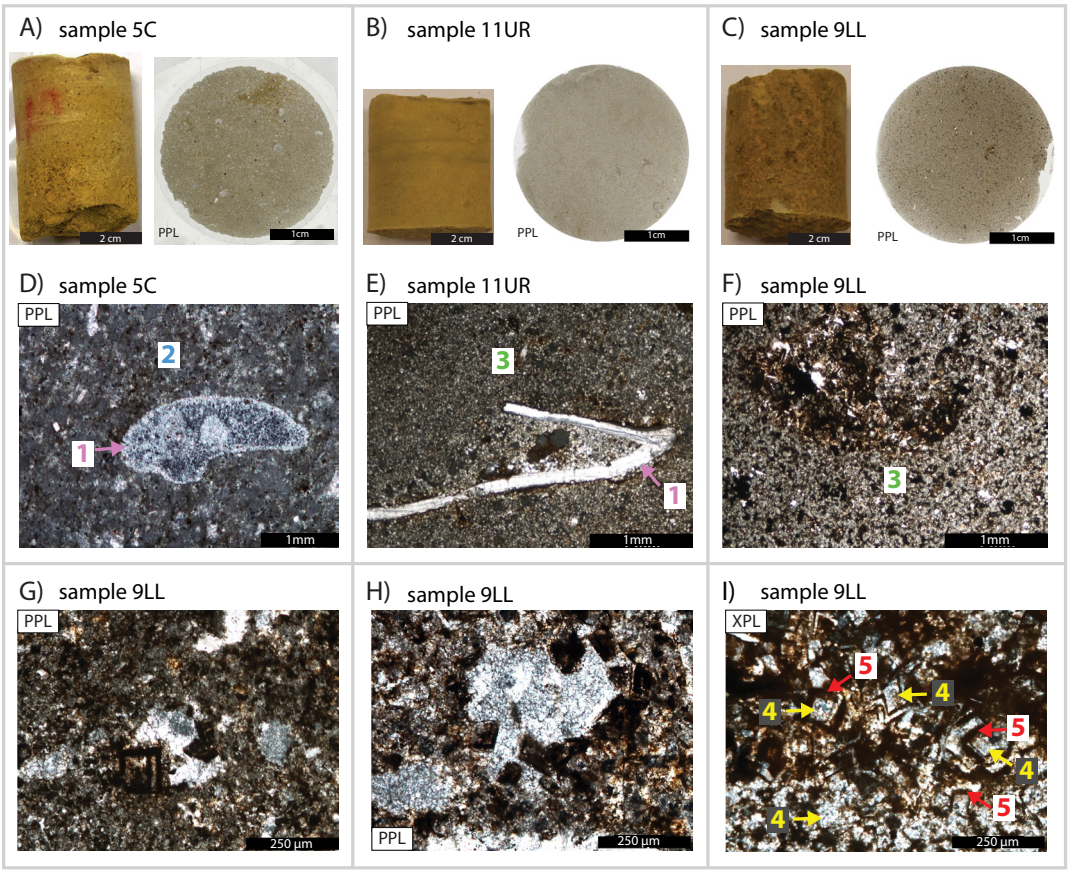

1=bioclast, 2=micritic matrix, 3=µm-scale sucrosic texture, 4=calcified dolomite petrographic rhombs, 5=ferric oxides and other opaque minerals, PPL=plane polarized light, XPL=cross polarized light

Figure 16. Petrographic images of samples 5C, 11UR, and 9LL show observations of dedolomitization processes in sample 9LL from combined laboratory analysis. Compare Table 1 for X-ray diffraction and grain density analysis of the plugs. (A–C) Photos of plug samples (left) and petrographic images shown as entire thin sections (right); (D–I) detailed thin section insets where (D) thin section of sample 5C (dolomite-free, 95% calcite by weight, low [2.68 g/cm^2] grain density) exhibits peloidal wackestone with sporadic bioclasts in a micritic matrix; (E) thin section of sample 11UR (96% dolomite by weight, high [2.76 g/cm^2] grain density) shows the micron-scale sucrosic texture typical of fully replacive dolomite; (F) thin section of sample 9LL (3% dolomite by weight, low grain density [2.67 g/cm^2]) exhibits micron-scale sucrosic textures; (G–I) zoomed thin sections of sample 9LL show calcified dolomite petrographic rhombs.

minerals occur within the inter-rhomb pore space and precipitated in remaining intracrystalline pores (Fig. 16I).

Dolomitization can produce locally enhanced porosity and permeability in carbonate rocks (Schoenherr et al., 2018). Subsequent percolation of mineralizing fluids can trigger calcite recrystallization of dolomites as well as silica and micron-scale crystal halite filling dolomite euhedral crystals through intracrystalline pores. The dolomite replacement with calcium at later diagenetic phases is accompanied by ferroan expulsion from dolomite crystal structure (mimicking the replacement of dolomite by calcite; fabric 1B according to Nader et al., 2008) and results in the formation of ferric oxides. High goethite concentrations (up to 250,000 ppm) are observed in sample S9LL based on quantitative mineral analysis of the thin section while the concentration of ferric oxide is high, and the concentration of dolomite is low. In the thin section of sample S11UR, the opposite ratio of ferric oxide and dolomite is observed; the lower the content of ferric oxides, the higher the content of ferroan dolomite. The thin section analysis confirms the limestone lithology of the brownish rock bodies, which are spectrally mapped as limestone, and explains the higher concentrations of iron oxides within recrystallized, formerly dolomitized limestone geobodies. For more detailed identification and mapping of ferric oxide, the VNIR spectral range would be required but was not available in this study.

As observed by Al-Hashimi and Hemingway (1973), and more recently by Beckert et al. (2015, 2018), brownish weathered limestone in hand samples and thin sections implies significant recrystallization processes. Beckert et al. (2018) studied the weathering and alteration of dolomite rocks in the Oman Mountains, which indicate challenges associated with hyperspectral interpretation. Weathering and alteration of dolomite rocks are often accompanied by the precipitation of goethite, hematite, specularite, and pyrite (Zeidan and Basyuni, 1998); however, reliable spectral mapping of these iron-bearing minerals is often challenging due to the low overall brightness and overprinting of other spectral signatures in mixed spectra. Early diagenetic dolomites exhibit randomly distributed concentrations of iron content (200 ppm to 12,000 ppm), which can be often observed as iron absorption in reflectance spectra (Fig. 12).

The adjacent occurrence of non-altered limestone and dolomitized limestone shown in Figures 11 and 15 can be explained by local variations in permeability. This allows variations in paleo-permeability to be interpreted and mapped using the hyperspectral results. Geobodies with the highest degree of dolomitization as well as the rock bodies occurring today as dedolomitized limestone are considered to have been more permeable than the unaltered limestone when the dolomitization occurred. The coexistence of highly dolomitized rock bodies and largely dedolomitized rock bodies may also be explained by variations in permeability. To what extent the geobodies spectrally mapped with intermediate dolomite contents and occurring adjacent to the highly dolomitized geologies (Figs. 10 and 15) result from early diagenetic dolomitization or from later diagenetic dedolomitization cannot be determined from the hyperspectral data alone. However, the hyperspectral maps are invaluable for guiding sample collection in future detailed diagenetic studies of the Alacón Member.

Mapping of Dolomite Bodies at Outcrop Scale

Figure 15B shows the distribution of highly dolomitized geobodies as identified by HSI. Areas where dolomite bodies were missed, or where dolomite content was overestimated, indicate the value of the technique for more detailed identification and semiquantitative mapping of the actual distribution of dolomite in outcrop characterization. Although it is outside the scope of this paper to fully reinterpret the diagenetic history of the Alacón Member, some changes to the earlier interpretation by Cepriá et al. (2002) are suggested, which indicate that the architecture of early diagenetic geobodies in the Alacón Member carbonate platform can be better defined.

The hyperspectral data indicate the strata-bound and non-fault-controlled nature of the original dolomite geobodies (Fig. 15; dolomite distribution is not controlled by fault planes mapped with red lines), which suggests that dolomitization affected practically the entire thickness of a bed when it occurred, with bedding planes acting as barriers for dolomitization fluxes. Examples can be observed where dolomitization developed from the top of a bed to the bottom, where the upper part exhibits the highest interpreted abundance of dolomite and basal parts show relatively low abundance (Fig. 15C). Based on the HSI mapping, we suggest that ephemeral and localized dolomitization fluxes resulted from single-phase and multi-event subaerial exposures of the Alacón carbonate ramp that are linked to high-frequency sea-level fluctuations during the Kimmeridgian rather than the single event related to one stratigraphic discontinuity proposed by Cepriá et al. (2002). However, future work is required to further the reconstruction of the paleo-presence of dolomite and, consequently, to better define the geometries and sedimentary architecture of the complete set of early diagenetic geobodies in Upper Jurassic carbonate platforms.

CONCLUDING REMARKS

The main findings of this study are summarized as follows.

(1) Hyperspectral mineral maps at outcrop scale have greatly enhanced our understanding of the spatial distribution of unaltered host limestone, dolomitized limestone, and iron-oxide–bearing limestone formed by the recrystallization processes of previously dolomitized geobodies in the Barranco del Mortero gully of Aragón, Spain. Integration of the detailed petrographic studies allowed reconstruction of the paleo-presence of dolomite and subsequent recrystallization.

(2) The study indicates that the Alacón Member contains significantly less dolomite than previously assumed from field geology. Previous studies missed some dolomite bodies or misclassified bodies as dolomite that later were found to be composed of limestone based on HSI and XRD. High-resolution hyperspectral mapping can therefore provide more detailed and reliable information about the distribution

of calcite and dolomite particularly in inaccessible cliff sections.

(3) To predict and quantify the degree of dolomitization from hyperspectral imaging, spectral measurements were calibrated using XRD sample measurements combined with a linear spectral mixing model. The resulting dolomite maps are affected by uncertainties related to (1) imprecise linkage between sample spots and spectral measurements in the hyperspectral imagery due to scale and spatial resolution issues; (2) limited spectral resolution of the hyperspectral imager; and (3) material mixtures resulting in modified material spectra.

(4) Comparing spectra from weathered and fresh sample surfaces indicates that weathered surfaces are representative and provide a good proxy for in situ geology in the outcrop studied. Spectral differences were minor compared to those of the spectra of fresh surfaces within this study.

(5) Hyperspectral maps are paramount for ensuring representative sampling of the outcrops. Analysis of the position and depth of the carbonate absorption features provides a useful basis for mapping as well as for indicating areas of uncertainty.

(6) The HSI-derived mineral maps provide realistic spatial trends of diagenetic products in carbonate rocks. This technique therefore has the potential to provide information that can be integrated for a better understanding of the sedimentology and diagenesis of carbonate platforms from outcrop models, which can be used as guides or proxies for subsurface reservoir characterization and 3-D upscaling of petrophysical properties in carbonate bodies.

ACKNOWLEDGMENTS

This research was funded by TotalEnergies SE. We thank TotalEnergies' laboratory at CSTJF Research and Scientific Centre and Panterra Geoconsultants (Pau, France), and especially Sergio Fernandez, for providing laboratory services. Benjamin Dolva processed ground-based photogrammetric 3-D models, and Nicole Naumann is thanked for several discussions on the hyperspectral processing. Kari Ringdal, Joris Vanbiervliet, and Bowei Tong are thanked for their work on the LIME software, which is also supported by the Research Council of Norway (SkatteFUNN project #266740). The authors are grateful to the geo-tourism park of Oliete for support during fieldwork.

REFERENCES CITED

Agar, S.M., and Geiger, S., 2014, Fundamental controls on fluid flow in carbonates: Current workflows to emerging technologies, *in* Agar, S.M., and Geiger, S., eds., Fundamental Controls on Fluid Flow in Carbonates: Geological Society, London, Special Publication 406, p. 1–59.

Al-Emadi, A., Jorry, S.-J., Chautru, J.-M., Caline, B., Blum, M.-S., Jedaan, N., Fryer, V., Leandri, P., and Fraisse, C., 2009, 3-D modeling of the Arab formation (Maydan Mahzam field, offshore Qatar): An integrated approach, *in* Proceedings, International Petroleum Technology Conference 13461, Doha, Qatar, 7–9 December 2009, 17 p.

Al-Hashimi, W.S., and Hemingway, J.E., 1973, Recent dedolomitization and the origin of the rusty crusts of Northumberland: Journal of Sedimentary Petrology, v. 43, p. 82–91, https://doi.org/10.1306/74D726E9-2B21-11D7-8648000102C1865D.

Asprion, U., and Aigner, T., 2000, An initial attempt to map carbonate buildups using ground penetrating radar: An example from the Upper Jurassic of SW-Germany: Facies, v. 42, p. 245–252, https://doi.org/10.1007/BF02562575.

Aurell, M., Mas, R., Melénde, Z.A., and Salas, R., 1994, El tránsito Jurásico-Cretácico en la Cordillera Ibérica: Relación tectónica-sedimentación y evolución paleogeográfica: Cuadernos de Geología Ibérica, v. 18, p. 369–396.

Bádenas, B., and Aurell, M., 2001, Kimmeridgian palaeogeography and basin evolution of northeastern Iberia: Palaeogeography, Palaeoclimatology, Palaeoecology, v. 168, p. 291–310, https://doi.org/10.1016/S0031-0182(01)00204-8.

Beckert, J., Vandeginste, V., and John, C.M., 2015, Exploring the geological features and processes that control the shape and internal fabrics of late diagenetic dolomite bodies (Lower Khuff equivalent—Central Oman Mountains): Marine and Petroleum Geology, v. 68, p. 325–340, https://doi.org/10.1016/j.marpetgeo.2015.08.038.

Beckert, J., Vandeginste, V., McKean, T.J., Alroichdi, A., and John, C.M., 2018, Ground-based hyperspectral imaging as a tool to identify different carbonate phases in natural cliffs: International Journal of Remote Sensing, v. 39, no. 12, p. 4088–4114, https://doi.org/10.1080/01431161.2018.1452068.

Bemis, S., Micklethwaite, S., Turner, D., James, M., Akciz, S., Thiele, S.T., and Bangash, H.A., 2014, Ground-based and UAV-based photogrammetry: A multi-scale, high-resolution mapping tool for structural geology and paleoseismology: Journal of Structural Geology, v. 69, no. A, p. 163–178.

Brigaud, B., Vincent, B., Pagel, M., Gras, A., Noret, N., Landrein, P., and Hurret, E., 2018, Sedimentary architecture, depositional facies and diagenetic response to intracratonic deformation and climate change inferred from outcrops for a pivotal period (Jurassic/Cretaceous boundary, Paris Basin, France): Sedimentary Geology, v. 373, no. 3, p. 48–76, https://doi.org/10.1016/j.sedgeo.2018.04.011.

Buckley, S.J., Howell, J.A., Enge, H.D., and Kurz, T.H., 2008, Terrestrial laser scanning in geology: Data acquisition, processing and accuracy considerations: Journal of the Geological Society, v. 165, no. 3, p. 625–638, https://doi.org/10.1144/0016-76492007-100.

Buckley, S.J., Enge, H.D., Carlsson, C., and Howell, J.A., 2010, Terrestrial laser scanning for use in virtual outcrop geology: The Photogrammetric Record, v. 25, no. 131, p. 225–239, https://doi.org/10.1111/j.1477-9730.2010.00585.x.

Buckley, S.J., Kurz, T.H., Howell, J.A., and Schneider, D., 2013, Terrestrial lidar and hyperspectral data fusion products for geological outcrop analysis: Computers & Geosciences, v. 54, p. 249–258, https://doi.org/10.1016/j.cageo.2013.01.018.

Buckley, S.J., Ringdal, K., Naumann, N., Dolva, B., Kurz, T.H., Howell, J.A., and Dewez, T.J.B., 2019, LIME: Software for 3-D visualization, interpretation, and communication of virtual geoscience models: Geosphere, v. 15, no. 1, p. 222–235, https://doi.org/10.1130/GES02002.1.

Burgess, P., 2013, CarboCAT: A cellular automata model of heterogeneous carbonate strata: Computers & Geosciences, v. 53, p. 129–140, https://doi.org/10.1016/j.cageo.2011.08.026.

Burton, D., Dunlap, D.B., Wood, L.J., and Flaig, P.P., 2011, Lidar intensity as a remote sensor of rock properties: Journal of Sedimentary Research, v. 81, p. 339–347, https://doi.org/10.2110/jsr.2011.31.

Cepriá, J.J., Bádenas, B., and Aurell, M., 2002, Sedimentary evolution and paleogeography of the Upper Jurassic (upper Kimmeridgian-Tithonian) in the Sierra de Arcos (Iberian Chain): Journal of Iberian Geology, v. 28, p. 93–106.

Chesley, J.T., Leier, A.L., White, S., and Torres, R., 2017, Using unmanned aerial vehicles and structure from motion photogrammetry to characterize sedimentary outcrops: An example from the Morrison Formation, Utah, USA: Sedimentary Geology, v. 354, p. 1–8, https://doi.org/10.1016/j.sedgeo.2017.03.013.

Clark, R.N., and Roush, T.L., 1984, Reflectance spectroscopy: Quantitative analysis techniques for remote sensing applications: Journal of Geophysical Research: Solid Earth, v. 89, p. 6329–6340, https://doi.org/10.1029/JB089iB07p06329.

Clark, R.N., King, T.V.V., Klejwa, M., Swayze, G.A., and Vergo, N., 1990, High spectral resolution reflectance spectroscopy of minerals: Journal of Geophysical Research: Solid Earth, v. 95, p. 12,653–12,680, https://doi.org/10.1029/JB095iB08p12653.

Clark, R.N., Swayze, G.A., Gallagher, A.J., King, T.V.V., and Calvin, W.M., 1993, The U.S. Geological Survey, Digital Spectral Library: Version 1: 0.2 to 3.0 μm: U.S. Geological Survey Open-File Report 93–592, 1326 p.

Crowley, J.K., 1986, Visible and near-infrared spectra of carbonate rocks: Reflectance variations related to petrographic texture and impurities: Journal of Geophysical Research: Solid Earth, v. 91, p. 5001–5012, https://doi.org/10.1029/JB091iB05p05001.

Denk, M., Gläßer, C., Kurz, T.H., Buckley, S.J., and Drissen, P., 2015, Mapping of iron and steelwork by-products using close range hyperspectral imaging: A case study in Thuringia, Germany: European Journal of Remote Sensing, v. 48, p. 489–509, https://doi.org/10.5721/EuJRS20154828.

Dravis, J.J., and Wanless, H.R., 2018, Reflux dolomitization—A Holocene example beneath a coastal salina, West Caicos Island, Turks and Caicos Islands: Marine and Petroleum Geology, v. 97, p. 311–322, https://doi.org/10.1016/j.marpetgeo.2018.07.003.

Franceschi, M., Teza, G., Preto, N., Pesci, A., Galgaro, A., and Girardi, S., 2009, Discrimination between marls and limestones using intensity data from terrestrial laser scanner: International Society for Photogrammetry and Remote

Sensing Journal of Photogrammetry and Remote Sensing, v. 64, no. 6, p. 522–528, https://doi.org/10.1016/j.isprsjprs.2009.03.003.

Gaffey, S.J., 1985, Reflectance spectroscopy in the visible and near infrared (0.35–2.55 microns): Applications in carbonate petrology: Geology, v. 13, p. 270–273, https://doi.org/10.1130/0091-7613(1985)13<270:RSITVA>2.0.CO;2.

Gaffey, S.J., 1986, Spectral reflectance of carbonate minerals in the visible and near infrared (0.35–2.55 microns): Calcite, aragonite, and dolomite: The American Mineralogist, v. 71, p. 151–162.

Grammer, G.M., Harris, P.M., and Eberli, G.P., 2004, Integration of outcrop and modern analogs in reservoir modeling: Overview with examples from the Bahamas, *in* Grammar, G.M., Harris, P.M., and Eberli, G.P., Integration of Outcrop and Modern Analogs in Reservoir Modeling: American Association of Petroleum Geologists Memoir, v. 80, p. 1–22.

Green, A.A., Berman, M., Switzer, P., and Craig, M.D., 1988, A transformation for ordering multispectral data in terms of image quality with implications for noise removal: IEEE Transactions on Geoscience and Remote Sensing, v. 26, p. 65–74, https://doi.org/10.1109/36.3001.

Hodgetts, D., 2013, Laser scanning and digital outcrop geology in the petroleum industry: A review: Marine and Petroleum Geology, v. 46, p. 335–354, https://doi.org/10.1016/j.marpetgeo.2013.02.014.

Hönig, M.R., and John, C.M., 2015, Sedimentological and isotopic heterogeneities within a Jurassic carbonate ramp (UAE) and implications for reservoirs in the Middle East: Marine and Petroleum Geology, v. 68, p. 240–257, https://doi.org/10.1016/j.marpetgeo.2015.08.029.

Hunt, G.R., and Salisbury, J.W., 1971, Visible and near-infrared spectra of minerals and rocks: II. Carbonates: Modern Geology, v. 2, no. 1, p. 23–30.

James, M.R., and Robson, S., 2012, Straightforward reconstruction of 3-D surfaces and topography with a camera: Accuracy and geoscience application: Journal of Geophysical Research: Earth Surface, v. 117, F03017, https://doi.org/10.1029/2011JF002289.

Jennings, J.W., 2000, Spatial statistics of permeability data from carbonate outcrops of West Texas and New Mexico: Implications for improved reservoir modeling: The Report of Investigations, University of Texas at Austin, Bureau of Economic Geology, v. 258, 50 p.

Kenter, J., Playton, T., Harris, P.M., Katz, D., and Bellian, J., 2010, Application of outcrop analogs to characterize carbonate reservoirs in the Pricaspian Basin, *in* Proceedings, SPE Caspian Carbonates Technology Conference, Atyrau: Kazakhstan, paper SPE-139934-MS, 13 p., https://doi.org/10.2118/139934-MS.

Kerans, C., Lucia, F.J., and Senger, R.K., 1994, Integrated characterization of carbonate ramp reservoirs using Permian San Andres Formation outcrop analogs: American Association of Petroleum Geologists Bulletin, v. 78, no. 2, p. 181–216.

Krupnik, D., Khan, S., Okyay, U., Hartzell, P., and Zhou, H.-W., 2016, Study of Upper Albian rudist buildups in the Edwards Formation using ground-based hyperspectral imaging and terrestrial laser scanning: Sedimentary Geology, v. 345, p. 154–167, https://doi.org/10.1016/j.sedgeo.2016.09.008.

Kruse, F., Lefkoff, A., Boardman, J., Heidebrecht, K., Shapiro, A., Barloon, P., and Goetz, A., 1993, The spectral image processing system (SIPS)—Interactive visualization and analysis of imaging spectrometer data: Remote Sensing of Environment, v. 44, p. 145–163, https://doi.org/10.1016/0034-4257(93)90013-N.

Kurz, T.H., Buckley, S.J., Howell, J.A., and Schneider, D., 2008, Geological outcrop modelling and interpretation using ground based hyperspectral and laser scanning data fusion: The International Archives of the Photogrammetry, Remote Sensing and Spatial Information Sciences, v. 37, no. B8, p. 1229–1234.

Kurz, T.H., Buckley, S.J., Howell, J.A., and Schneider, D., 2011, Integration of panoramic hyperspectral imaging with terrestrial lidar data: The Photogrammetric Record, v. 26, no. 134, p. 212–228, https://doi.org/10.1111/j.1477-9730.2011.00632.x.

Kurz, T.H., Dewit, J., Buckley, S.J., Thurmond, J.B., Hunt, D.W., and Swennen, R., 2012, Hyperspectral image analysis of different carbonate lithologies (limestone, karst and hydrothermal dolomites): The Pozalagua Quarry case study (Cantabria, North-west Spain): Sedimentology, v. 59, no. 2, p. 623–645, https://doi.org/10.1111/j.1365-3091.2011.01269.x.

Kurz, T.H., Buckley, S.J., and Howell, J.A., 2013, Close-range hyperspectral imaging for geological field studies: Workflow and methods: International Journal of Remote Sensing, v. 34, no. 5, p. 1798–1822, https://doi.org/10.1080/01431161.2012.727039.

Kurz, T.H., Buckley, S.J., and Becker, J.K., 2017, Hyperspectral imaging: A novel geological mapping technique for subsurface construction sites, *in* Proceedings of the World Tunnel Congress 2017—Surface challenges—Underground Solutions: Bergen, Norway, Norwegian Tunnelling Society, 10 p.

Lindsay, R.F., Cantrell, D.L., Hughes, G.W., Keith, T.H., Mueller, H.W., and Russell, D., 2006, Ghawar Arab-D reservoir: Widespread porosity in shoaling-upward carbonate cycles *in* Harris, P.M., and Weber, L.J., eds., Giant Hydrocarbon Reservoirs of the World: From Rocks to Reservoir Characterization and Modeling: American Association of Petroleum Geologists Memoir 88/Society for Sedimentary Geology (SEPM) Special Publication, p. 97–137.

Lorenz, S., Salehi, S., Kirsch, M., Unger, G., Sørensen, E., Gloaguen, R., and Zimmermann, R., 2018, Radiometric correction and 3-D integration of long-range ground-based hyperspectral imagery for mineral exploration of vertical outcrops: Remote Sensing, v. 10, p. 176, https://doi.org/10.3390/rs10020176.

Machel, H.G., 2004, Concepts and models of dolomitization: A critical reappraisal, *in* Braithwaite, C.J.R., Rizzi, G., and Darke, G., eds., The Geometry and Petrogenesis of Dolomite Hydrocarbon Reservoirs: Geological Society, London, Special Publication 235, p. 7–63, https://doi.org/10.1144/GSL.SP.2004.235.01.02.

Morad, S., Al-Aasm, I.S., Nader, F.H., Ceriani, A., Gasparrini, M., and Mansurbeg, H., 2012, Impact of diagenesis on the spatial and temporal distribution of reservoir quality in the Jurassic Arab D and C Members, offshore Abu Dhabi oilfield, United Arab Emirates: GeoArabia, v. 17, no. 3, p. 17–56.

Murphy, R.J., Schneider, S., and Monteiro, S.T., 2014, Mapping layers of clay in a vertical geological surface using hyperspectral imagery: Variability in parameters of SWIR absorption features under different conditions of illumination: Remote Sensing, v. 6, p. 9104–9129, https://doi.org/10.3390/rs6099104.

Nader, F.H., Swennen, R., and Keppens, E., 2008, Calcitization/dedolomitization of Jurassic dolostones (Lebanon): Results from petrographic and sequential geochemical analyses: Sedimentology, v. 55, p. 1467–1485, https://doi.org/10.1111/j.1365-3091.2008.00953.x.

Nader, F.H., De Boever, E., Gasparrini, M., Liberati, M., Dumont, C., Ceriani, A., Morad, S., Lerat, O., and Doligez, B., 2013, Quantification of diagenesis impact on the reservoir properties of the Jurassic Arab D and C members (Offshore, U.A.E.): Geofluids, v. 13, p. 204–220, https://doi.org/10.1111/gfl.12022.

Schoenherr, J., Reuning, L., Hallenberger, M., Lüders, V., Lemmens, L., Biehl, B.C., Lewin, A., Leupold, M., Wimmers, K., and Strohmenger, C.J., 2018, Dedolomitization: Review and case study of uncommon mesogenetic formation conditions: Earth-Science Reviews, v. 185, p. 780–805, https://doi.org/10.1016/j.earscirev.2018.07.005.

Smith, M.G., and Milton, J.E., 1999, The use of the empirical line method to calibrate remotely sensed data to reflectance: International Journal of Remote Sensing, v. 20, p. 2653–2662, https://doi.org/10.1080/014311699211994.

Swart, P.K., Cantrell, D.L., Westphall, H., Handford, C.R., and Kendall, C.G., 2005, Origin of dolomite in the Arab-D reservoir from the Ghawar field, Saudi Arabia: Evidence from petrographic and geochemical constraints: Journal of Sedimentary Research, v. 75, p. 476–491, https://doi.org/10.2110/jsr.2005.037.

Van der Meer, F., 1995, Spectral reflectance of carbonate mineral mixtures and bidirectional reflectance theory: Quantitative analysis techniques for application in remote sensing: Remote Sensing Reviews, v. 13, p. 67–94, https://doi.org/10.1080/02757259509532297.

van der Meer, F., 2004, Analysis of spectral absorption features in hyperspectral imagery: International Journal of Applied Earth Sciences and Geoinformation, v. 5, p. 55–68, https://doi.org/10.1016/j.jag.2003.09.001.

van Koppen, J., Al-Menhali, H., Alblooshi, A., Caline, B., Guy, L., Kheidri, H., Hu, T., Kwasniewski, A., Dubois, L., San Miguel, G., Duval, C., Deviese, E., Thomas, E., Vanhalst, M., Dreno, C., Mel, R., and Elhami, M., 2015, Geological mapping of early diagenetic bodies as a tool to distribute permeability in a mature giant carbonate field, Abu Dhabi, *in* Proceedings, International Petroleum Exhibition and Conference 2015: Society of Petroleum Engineers, paper SPE-177850-MS, 12 p., https://doi.org/10.2118/177850-MS.

Warren, J., 2000, Dolomite: Occurrence, evolution and economically important associations: Earth-Science Reviews, v. 52, p. 1–81, https://doi.org/10.1016/S0012-8252(00)00022-2.

Zaini, N., van der Meer, F., and van der Werff, H., 2012, Effect of grain size and mineral mixing on carbonate absorption features in the SWIR and TIR wavelength regions: Remote Sensing, v. 4, p. 987–1003, https://doi.org/10.3390/rs4040987.

Zeidan, R.H., and Basyuni, M.H., 1998, Modes of occurrence of dolomite in some Arabian carbonate rocks: Journal of King Abdulaziz University, v. 10, p. 1–16, https://doi.org/10.4197/Ear.10-1.1.